

Hydrogen under Pressure as a Benchmark for Machine-Learning Interatomic Potentials

Thomas Bischoff¹, Bastian Jäckl¹, Matthias Rupp²

¹ Department of Computer and Information Science, University of Konstanz, Konstanz, Germany ² Luxembourg Institute of Science and Technology (LIST), Esch-sur-Alzette, Luxembourg

Abstract

Machine-learning interatomic potentials (MLPs) are fast, data-driven surrogate models of atomistic systems' potential energy surfaces that can accelerate ab-initio molecular dynamics (MD) simulations by several orders of magnitude. The performance of MLPs is commonly measured as the prediction error in energies and forces on data not used in their training. While low prediction errors on a test set are necessary, they do not guarantee good performance in MD simulations. The latter requires physically motivated performance measures obtained from running accelerated simulations. However, the adoption of such measures has been limited by the effort and domain knowledge required to calculate and interpret them.

To overcome this limitation, we present a benchmark that automatically quantifies the performance of MLPs in MD simulations of a liquid-liquid phase transition in hydrogen under pressure, a challenging benchmark system. The benchmark's `h-11pt-24` dataset provides reference geometries, energies, forces, and stresses from density functional theory MD simulations at different temperatures and mass densities. The benchmark's Python code automatically runs MLP-accelerated MD simulations and calculates, quantitatively compares and visualizes pressures, stable molecular fractions, diffusion coefficients, and radial distribution functions. Employing this benchmark, we show that several state-of-the-art MLPs fail to reproduce the liquid-liquid phase transition.

Contents

1	Introduction	3
2	Background	4
3	Related work	5
4	Dataset	5
5	Performance measures	7
6	Benchmark	9
7	Results and discussion	9
8	Conclusions	12
	Acknowledgments	12
	Data and code availability	12
	References	12

Supplementary information **16**

A	Computational details	16
A.1	Molecular dynamics simulations	16
A.2	Molecular dynamics-derived properties and post-processing	17
A.3	Training of machine learning interatomic potentials	17
B	Analysis details	18
B.1	Derived properties	18
B.2	Scatter plots	18
B.3	Hellinger distances	18
	References	31

1 Introduction

Molecular dynamics (MD) simulations of atomistic systems are a cornerstone of computational physics, chemistry, and materials science, but are limited by either accuracy or computational cost. The trade-off between accuracy and cost is determined by the method used to compute the system’s potential energy, whose negative gradient are the forces that propagate atoms in the simulation.

Typical choices include classical force fields, characterized by fixed functional forms, and quantum-mechanical (*ab initio*) approaches. Force fields are computationally efficient but limited in accuracy, transferability, and by parametrization effort. *Ab initio* approaches are accurate and transferable but have high computational costs. Consequently, MD simulations are limited in either the phenomena (e.g., bond breaking and formation) or the system sizes and time scales they can model.

Machine-learning interatomic potentials (MLPs)¹ are data-driven approximations of *ab-initio* potential energy surfaces that exploit correlations between the atom positions and the potential energy of a system. Essentially, a flexible functional form such as a neural network is parametrised (“trained”) on a dataset of *ab initio* calculations. The parametrised model then calculates the forces during a simulation. MLPs are typically several orders of magnitude faster to evaluate than the *ab initio* reference method.^{2;3} This greatly accelerates MD simulations, enabling running more simulations, simulating larger systems, and increasing simulation times, resulting in improved configurational sampling, property estimates, and the ability to model otherwise inaccessible phenomena.

MLP-accelerated MD simulations should reproduce the results of corresponding *ab-initio* MD simulations. More specifically, the discrepancies in derived macroscopic quantities, such as radial distribution functions and diffusion coefficients, should be as small as possible. The MLP-MD should also reproduce any monotony, limits, and asymptotic behaviour of such quantities. This is necessary to consistently describe physical phenomena such as proton exchange and phase transitions. Validation and performance assessment of MLPs for MD should therefore base on MLP-accelerated MD simulations.

In practice, MLP performance is commonly evaluated as the average error in force predictions on a test dataset (data not used during training but from the same distribution as the training data), without involving any MD simulations. However, force accuracy on a test set is necessary but insufficient for successful MD simulations.⁴⁻⁷ Consequently, MLPs with reported state-of-the-art test-set accuracy can fail catastrophically in actual MD simulations.

The inadequacy of test-set force errors as the sole performance indicator for MD simulations is increasingly recognized in the community. Despite this, the uptake of assessment methods based on MLP-MD simulations is slow, possibly because these require more human and computational effort as well as expert domain knowledge of the simulated system and the derived properties.

In this work, we introduce an MD-based benchmark of MLP performance that is straightforward to use and does not require expert domain knowledge. For this we employ simulation of a liquid-liquid phase transition in hydrogen under pressure as a challenging application. The benchmark provides the `h-llpt-24` dataset with geometries, energies, forces, and stresses from reference MD simulations at the density functional level of theory for different temperatures and mass densities. This data serves as training, validation, and testing data for MLP parametrisation.

Once parametrised, the benchmark’s Python code automatically runs MLP-accelerated MD simulations and calculates and visualises pressures, stable molecular fractions, diffusion coefficients, and radial distribution functions as functions of cell density. These MD-derived properties characterise the liquid-liquid phase transition and are quantitatively compared with those from the reference simulations. Outputs include automatically generated figures and tables. We employ the benchmark to show that several state-of-the-art MLPs fail to reproduce the liquid-liquid phase transition.

The benchmark (a) focuses on learning a single potential energy surface, as opposed to generalising across multiple atomistic systems simultaneously;⁸ (b) focuses on learning the map from local atomic geometry to energy; in particular, it does not measure an MLP’s ability to model different chemical elements; (c) provides physical system-specific derived properties as performance metrics, beyond generic performance metrics; (d) resolves differences between MLPs well due to the high difficulty of the learning task.

2 Background

Hydrogen under pressure. The term warm dense matter refers to atomistic systems in a regime of temperature and density between the condensed phase and hot plasma. Warm dense hydrogen (WDH) exhibits complex behaviour, including multiple solid and liquid phases and the transitions between them.⁹ These are relevant, among others, for modelling gas planets,¹⁰ high-pressure physics, hydrogen-based inertial confinement fusion, and the design of hydrogen-rich materials.

The phase diagram of WDH has been intensely debated in the literature for almost a century. There are multiple reasons for disagreements: Experimental synthesis and characterisation of WDH are challenging due to the high temperatures and pressures involved.¹¹ Challenges of computational approaches include WDH’s many-body quantum nature, high computational costs, and limits of the approximations used, for example, strong dependency on the exchange-correlation functional^{9;12}.

This work focuses on a liquid-liquid phase transition (LLPT) between molecular and atomic liquid hydrogen, using density-functional theory (DFT) with the Perdew-Burke-Ernzerhof (PBE)¹³ functional as the ground truth. In this, our aim is not further insight into the LLPT itself. Instead, we use modelling of the LLPT at the DFT/PBE level of theory as a hard and therefore discriminating benchmark for MLPs.

While the nature of the LLPT in WDH remains under debate,^{14–16} computational studies^{9;12;15;17–22} indicate a first-order transition. This is also the case for the DFT/PBE method used in this work. Such a transition is characterised by a sudden discontinuous change in observables, including pressure, stable molecular fraction, diffusion coefficient, and radial distribution function as a function of density. These observables can be estimated from MD simulations of WDH.

Molecular dynamics simulations²³ enable observing the evolution of an atomistic system over time and, based on this, calculating derived properties of that system. For every time step of the simulation, each atom’s position is updated based on its mass, velocity, and the force acting on it. As the force is the negative gradient of the potential energy with respect to atom position, this requires a potential energy function, or potential, that calculates the potential energy of a system given the position and chemical species of its atoms.

The computational cost of an MD simulation scales with the number of atoms and time steps. Extended systems are often approximated by simulating a smaller part, the unit cell, with periodic boundary conditions. While this saves computational cost, the unit cell cannot be too small, as this would lead to finite-size effects.

For long simulations of large systems, it is therefore important that the potential is efficient to evaluate. Traditional empirical potentials have fixed functional forms that allow for efficient evaluation but limit accuracy. Ab-initio potentials solve the quantum-mechanical equations governing the system, leading to accurate forces but high computational costs. Data-driven potentials offer a compromise, see Section 2.

Some thermodynamic variables are held constant during an MD simulation to imitate real-world conditions. In the canonical ensemble (NVT), the number of atoms N , the volume V of the unit cell and the temperature T are held constant. The latter is controlled via a thermostat that adjusts the kinetic energy of the atoms.

Machine-learning interatomic potentials¹ are computationally efficient, data-driven approximations of ab-initio potential-energy surfaces. Their computational costs typically fall between those of traditional empirical potentials and those of ab-initio potentials. Their approximation error determines how well they can reproduce the physics in an MD simulation and, thus, the accuracy of the derived observables. Many types of MLPs have been developed. They differ, among other aspects, in the interactions they model, how they featurise these, and the regression algorithm used.

Global MLPs consider all interactions between atoms; for this reason, they usually scale superlinearly with system size. To scale linearly, most MLPs consider only finite subsets of interactions. Typically, such local MLPs for each atom consider only interactions with neighbouring atoms within a given distance. Semilocal MLPs build up longer-range correlations iteratively from local ones, often through message-passing mechanisms. Interactions between atoms are numerically represented (“featurised”) for regression. Corresponding basis functions are either explicitly given or learned from the training data. Popular regression algorithms include linear regression, kernel regression, and neural networks.

3 Related work

Benchmarks for MLPs typically report prediction errors for energies and forces on test sets, that is, data sampled from the same distribution as the training data but not used for training the MLP. As prediction errors are straightforward to compute, these benchmarks provide reference data but not program code to calculate or visualise performance metrics. Popular datasets for benchmarking MLPs include QM7^{8;24}, QM9²⁵, MD17^{26;27}, and OC20^{28;29}. See Vita et al.³⁰ for a recent collection of such datasets.

The need for validation of MLPs beyond test-set prediction errors has been recognised in the community for several years. Only recently, however, have systematic efforts been made to address this problem:

Stocker et al.⁵ investigate the robustness of the GemNet³¹ MLP, trained on the QM7-x²⁴ dataset of small organic molecules, in long dynamics simulations (280 ns total simulation time). They find that “low test set errors are not sufficient for obtaining stable dynamics and that severe pathologies sometimes only become apparent after hundreds of ps of dynamics.” Their study focuses on stability and does not investigate properties derived from simulations.

Fu et al.⁶ benchmark nine MLPs on water, small organic molecules, alanine dipeptide, and $\text{Li}_{6.75}\text{P}_3\text{S}_{11}$. They find that “force accuracy alone does not suffice for effective simulation.” For alanine dipeptide, the only MLP stable over five nanoseconds of simulation time failed to reproduce its free energy surface. Their benchmark provides simulation protocols, an open-source codebase,³² and quantitative metrics for derived properties, specifically interatomic distance distributions, radial distribution functions, diffusion coefficients, free energies, and simulation stability. The benchmark in this work includes two of these generic metrics, radial distribution functions and diffusion coefficients, but also provides application-specific metrics related to the LLPT of hydrogen under pressure.

Fonseca et al.³³ provide the cross-platform software package FFAST (Force Field Analysis Software and Tools) to benchmark, analyse, and visualise MLP performance and limitations. They demonstrate their software for the Nequip³⁴ and MACE³⁵ MLPs applied to stachyose and docosahexaenoic acid. Their approach is geared towards molecules, that is, multi-element systems where covalent bonding dominates and does not change much. Consequently, many analysis features do not apply to our setting, such as element-resolved error distributions or identification of specific atoms with higher prediction errors. Where applicable, we adapt features, such as error distribution plots.

Morrow et al.⁷ discuss best practices for validating MLPs but do not provide specific benchmarks. We follow their guidance where appropriate. In particular, we evaluate MLPs only with respect to the ground-truth ab-initio method that generated the training data, as comparing with experimental results would evaluate the suitability of the reference method instead of the suitability of the MLP. They conclude that it would be “desirable to create openly available ‘packaged’ tests that can be run directly from an openly available and easily accessible code, say, a Python script or automated workflow,” which this benchmark provides.

In active learning,³⁶ an MLP is dynamically (“on the fly”³⁷) retrained during an accelerated MD simulation whenever it encounters a system configuration outside its domain of applicability. Since reference calculations are only done when required for the MD, active learning is a more data-efficient alternative to static MLPs trained on a fixed training set and to extending the training set via unbiased sampling from MD trajectories. In this work, we do not employ active learning as it would (a) introduce additional requirements for MLPs, such as predictive uncertainties; (b) introduce additional factors influencing MLP performance, such as the active learning algorithm; and (c) substantially complicate benchmarking by tightly coupling training to simulations.

4 Dataset

The benchmark is based on the **h-11pt-24** dataset introduced below. This dataset contains 612 DFT reference MD simulations of 10k steps each. Part of this data is provided for training, validating, and testing MLPs. All data (after equilibration) was used to calculate reference values for the MD-derived properties in Section 5.

We constructed the **h-11pt-24** dataset explicitly to benchmark MLPs. Its complexity does not come from interactions of multiple chemical elements but solely from the non-linearity of interactions between its particles. In particular, the effects of partially bound electrons have to be detected indirectly from the hydrogen nuclei’s positions. As such, this setting primarily tests an MLP’s ability to learn complex high-dimensional functions.

To generate the `h-11pt-24` dataset, we ran ab-initio MD simulations of 128 hydrogen atoms in a cubic unit cell under periodic boundary conditions at different temperatures and densities (Figure 1, Table SI1). For each of the six temperatures T , we chose 17 equally-spaced Wigner-Seitz radii r_s , covering the regime of the LLPT. We ran six MD simulations for each combination (T, r_s) , resulting in a total of $6 \cdot 17 \cdot 6 = 612$ MD simulations. These simulations were performed in the NVT ensemble, using DFT with the PBE¹³ functional as the potential, and were carried out using the `Quantum ESPRESSO`^{38;39} software. To decorrelate configurations, we subsampled each simulation’s trajectory, taking two configurations from early in the 0.5 ps equilibration phase and 12 configurations at regularly-spaced intervals of 40 fs after equilibration.

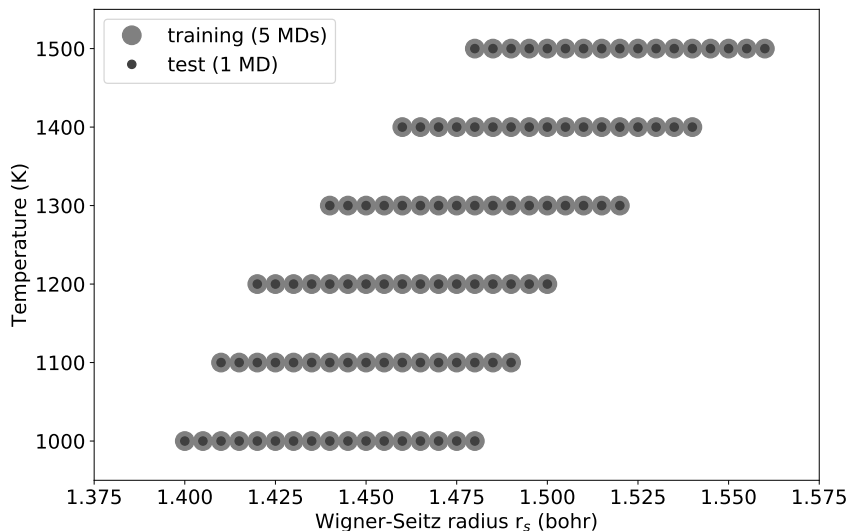


Figure 1: *Dataset coverage.* Each disk represents a combination of Wigner-Seitz radius and temperature for which six DFT MD simulations were performed, five for training of MLPs and one for testing.

This resulted in 8568 configurations, which we split into a training set of 7140 and a test set of 1428 configurations. The training configurations were sampled from five of the six repetitions; the test configurations were sampled from the remaining trajectory. Training and test data are thus sampled independently from the same distribution, satisfying the underlying assumption of machine-learning models that data are independent and identically distributed.

If a validation set is desired for MLP training, e.g., for early stopping or hyperparameter optimisation, the training set can be split further into a (smaller) training set and a validation set following the same approach: One of the five trajectories is used for validation, and the other four are used for training. Similarly, the trajectory designations can also be used for five-fold cross-validation.

For each configuration, the dataset provides lattice vectors (\AA), atom positions (\AA), total energy (eV), forces (eV/\AA), stress tensor (eV/\AA^3), pressure (GPa), Wigner-Seitz radius (bohr), temperature (K), and trajectory number (unitless). Figure 2 presents the distribution of energies, forces, and pressures in the training, validation (`md=4`), and test sets. For further computational details, see Appendix A.

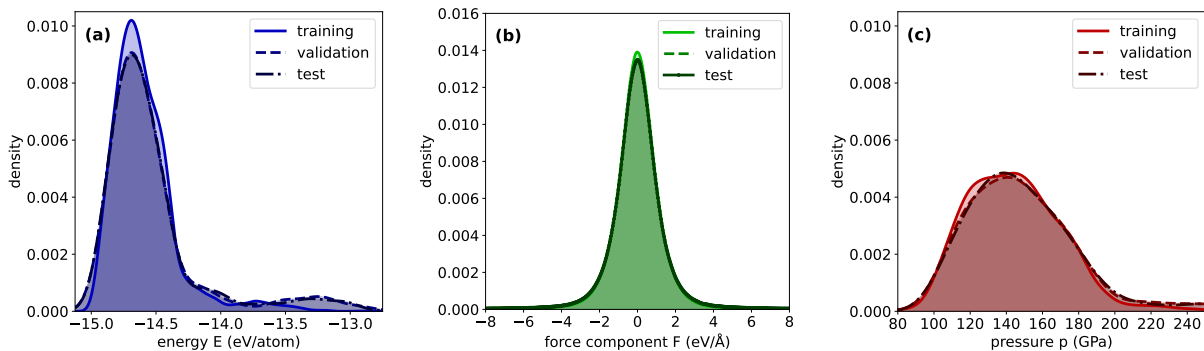


Figure 2: *Distribution of energies, forces, and pressures* in the `h-11pt-24` dataset. Shown are smoothed histograms of energies (left), forces (middle), and pressures (right) in the training (solid), validation (dashed), and test (dotted) subsets.

5 Performance measures

The benchmark uses four MD-derived properties to quantify the performance of MLPs in characterising the LLPT of WDH. This requires running and analysing MD simulations. To facilitate this, it provides Python scripts that automatically run multiple MD simulations, calculate the derived properties including uncertainties (error bars), and visualise them. When comparing with the DFT-MD ground truth, these uncertainties are taken into account via the Hellinger distance.

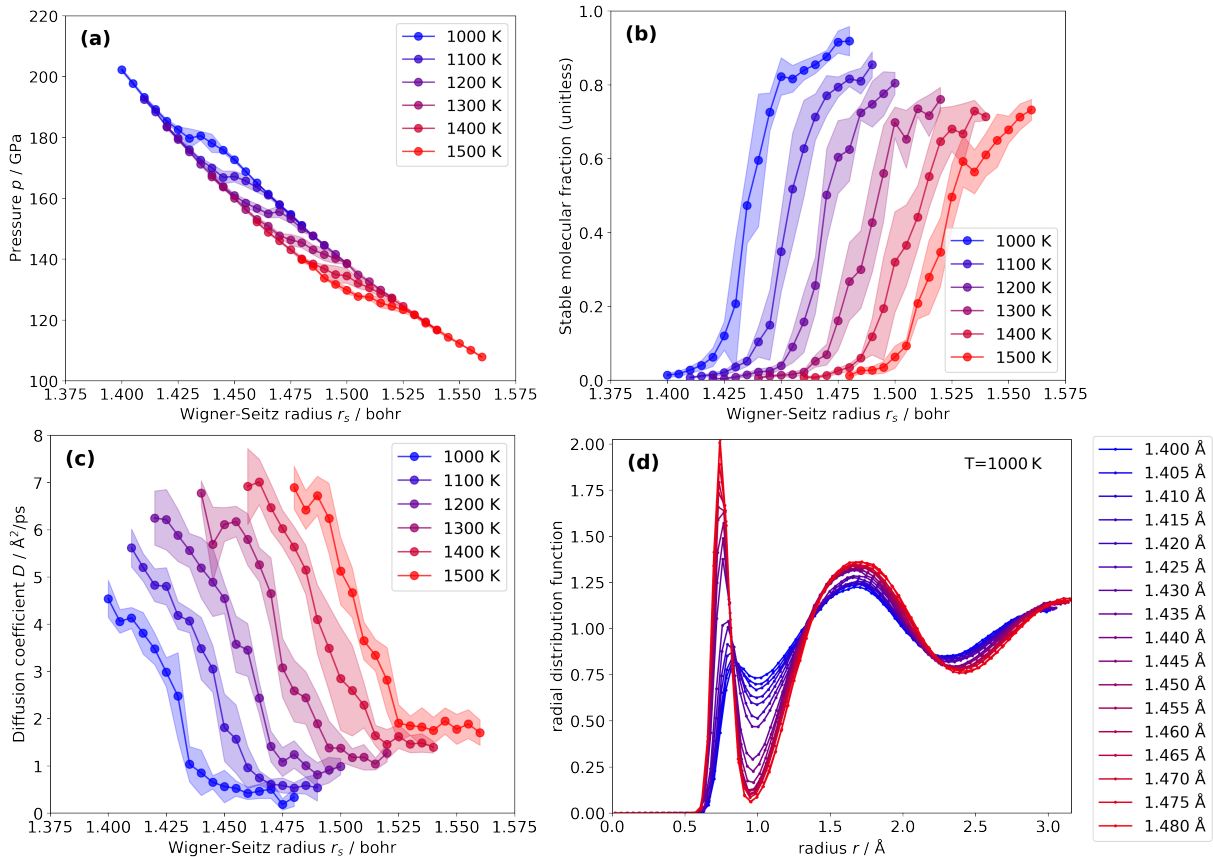


Figure 3: *Derived properties* based on the reference DFT/PBE MD simulations of the h-11pt-24 dataset. Shown are (a) pressure, (b) stable molecular fraction, and (c) diffusion coefficient as a function of the Wigner-Seitz radius r_s and for different temperatures (color-coded), as well as (d) radial distribution functions at 1000 K for different Wigner-Seitz radii (color-coded).

Pressure curves show isotropic pressure as a function of the Wigner-Seitz radius r_s at different temperatures (Figure 3a). These curves relate the state variables temperature, pressure, and density, effectively corresponding to equations of state. For pure atomic and molecular phases, pressure decreases monotonically with r_s . Near the LLPT, pressure remains almost constant, leading to a characteristic plateau. This effect decreases for higher temperatures. While the existence, explanation, and position of the actual plateaus depend on the ab-initio method and have been controversially debated, results reported in the literature for DFT-PBE are consistent.^{12;14;15;18;19;22;40–42} The benchmark measures the ability of an MLP to reproduce the DFT-PBE results.

Stable molecular fractions μ indicate the fraction of hydrogen atoms that form an H_2 dimer for an extended time span. Specifically, we consider two hydrogen atoms to be a stable dimer if they remain within 0.95 Å of each other for at least 75 fs. These thresholds reflect the typical time and length scales in WDH.¹² Moreover, we find that the inflection point of the isothermal μ over r_s curve is not sensitive to the choice of thresholds. The benchmark calculates μ for each trajectory frame and reports the average. In the atomic liquid phase, μ is (close to) zero, whereas in the molecular liquid phase, μ is (close to) one. The transition between the two phases is visible as a sudden change in μ (Figure 3b).

The (self-)diffusion coefficient D quantifies the mobility of the hydrogen atoms. The benchmark code first computes the 3×3 diffusion tensor \mathbf{D} from the squared displacements of the atomic positions via

the Einstein equation⁴³

$$\mathbf{D} = \frac{1}{2} \lim_{t \rightarrow \infty} \frac{\partial}{\partial t} \frac{1}{N} \sum_{i=1}^N (\mathbf{r}_i(t) - \mathbf{r}_i(0))^2, \quad (1)$$

where N is the number of atoms in the unit cell and $\mathbf{r}_i(t)$ is the position of atom i at time t . Averaging the main diagonal then yields $D = \frac{1}{3}(\mathbf{D}_{1,1} + \mathbf{D}_{2,2} + \mathbf{D}_{3,3})$. For homogeneous systems, the tensor's main diagonal elements should be similar, and the off-diagonal elements should be small.

Equation 1 converges for large enough N and t . While in this benchmark, N and t are too small for convergence, they are large enough to facilitate the comparison between DFT and MLPs, and to indicate the observed LLPT: The atomic phase is characterised by highly mobile hydrogen atoms, and thus large D , whereas the molecular phase exhibits a more viscous behaviour, and thus smaller D . The transition between the two phases is visible as a sudden change in D (Figure 3c).

The **radial distribution function (RDF)** $g(r)$, also called pair correlation function, describes the average density of hydrogen atoms as a function of distance from a hydrogen atom. For a homogeneous and isotropic system, the RDF is measured relative to the system's overall density N/V , where N is the number of atoms and V is the volume of the unit cell. The benchmark computes the RDF as a histogram by counting the atoms in spherical shells around a central atom and dividing by the shells' volumes $\frac{4}{3}\pi(r + \Delta)^3 - \frac{4}{3}\pi r^3$, where r is the distance at which the shell starts and Δ is its thickness. Together,

$$g(r, \Delta) = \left(\frac{1}{N} \sum_{i,j=1}^N [r \leq \|\mathbf{r}_j - \mathbf{r}_i\| \leq r + \Delta] \right) / \frac{N}{V} \frac{4}{3}\pi((r + \Delta)^3 - r^3),$$

where $[\dots]$ are Iverson brackets, \mathbf{r}_i is the position of atom i , and $\|\cdot\|$ is Euclidean distance under periodic boundary conditions. The molecular liquid shows a peak at the hydrogen-hydrogen bonding distance, whereas the atomic liquid does not (Figure 3d). For larger distances, the RDF converges to the ideal gas limit.

The benchmark uses the **Hellinger distance (HD)**⁴⁴ to quantify the discrepancies between properties derived from reference DFT and MLP-accelerated MD simulations. This statistical measure quantifies the similarity between two probability distributions. It is closely related to the Bhattacharyya coefficient⁴⁵ but is a metric in the mathematical sense: It is non-negative, symmetric, and obeys the triangle inequality. Furthermore, it is bounded between 0 and 1, with 0 (1) representing perfect (vanishing) overlap between two distributions. Figure 4 presents a graphical illustration of the HD.

The benchmark assumes that property values derived from multiple MD simulations are normally distributed. The HD of two scalar, normally distributed random variables $f_{\text{DFT}} \sim \mathcal{N}(\mu_{\text{DFT}}, \sigma_{\text{DFT}})$ and $f_{\text{MLP}} \sim \mathcal{N}(\mu_{\text{MLP}}, \sigma_{\text{MLP}})$ is

$$\text{HD}(f_{\text{MLP}}, f_{\text{DFT}}) = \sqrt{1 - \sqrt{\frac{2\sigma_{\text{MLP}}\sigma_{\text{DFT}}}{\sigma_{\text{MLP}}^2 + \sigma_{\text{DFT}}^2}} \exp\left(-\frac{1}{4} \frac{(\mu_{\text{MLP}} - \mu_{\text{DFT}})^2}{\sigma_{\text{MLP}}^2 + \sigma_{\text{DFT}}^2}\right)}. \quad (2)$$

For multivariate quantities, the benchmark averages over the HDs between components.

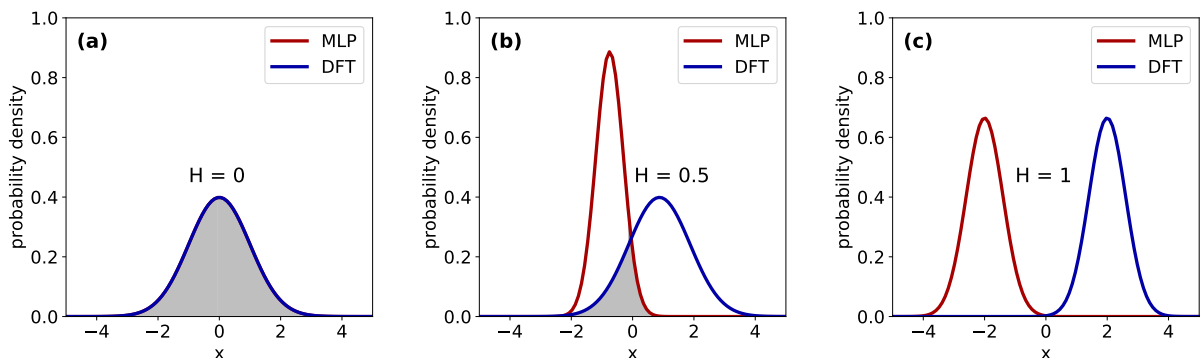


Figure 4: *Illustration of the Hellinger distance.* Shown are (a) perfect, (b) intermediate, and (c) vanishing overlap of two one-dimensional distributions (MLP, DFT). The intersection is shown in gray.

Test-set prediction errors. We also provide the error in predicted energies and forces on a dedicated test dataset sampled from the same distribution as the training data (Section 4). These test-set errors can provide insights into an MLP and its failure modes, e.g., via bias and outlier analysis. However, test-set errors are not necessarily indicative of the accuracy of MD-derived properties (Section 3).

For test-set predictions of energies and (component-wise) forces, we report the mean absolute error (MAE), root-mean-squared error (RMSE), and maximum absolute error, both as-is and as fractions of their respective ranges, as well as $\log(1 - R^2)$, where R is Pearson’s correlation coefficient, a measure of linear correlation. For simplicity, we refrain from adjusting the range for outlying values and from dividing by standard deviation instead of range.

For visual analysis the benchmark provides scatter plots of predicted versus ground-truth values. These plots also show the distribution of predicted and ground-truth DFT energies and force components, as well as log-log histograms of prediction errors. See Figures 6 and SI3 for examples.

6 Benchmark

Benchmarking the performance of an MLP in characterising the LLPT of WDH consists of these steps:

- (1) Training the MLP on the `h-11pt-24` dataset, using only the training data part.
- (2) Running MD simulations with the trained MLP.
- (3) Calculating derived properties (Section 5) based on the generated trajectories.
- (4) Comparing these with the properties obtained from the DFT reference simulations via the HD.

Step (1) depends on the specifics of the MLP and is, therefore, not performed by the benchmark code. All other steps, (2), (3), and (4), do not depend on the specifics of the MLP and are fully automatised by the benchmark code.

Step (2) runs multiple MD simulations in the *NVT* ensemble with the same settings as in Section 4 but using the MLP instead of the DFT potential energy surface. Specifically, for each of the six temperatures and 17 Wigner-Seitz radii, 12 independent MD simulations are performed, resulting in a total of $6 \cdot 17 \cdot 12 = 1\,224$ MD simulations. Of the 10k time steps in each simulation, the first 2500 time steps are discarded to allow for equilibration. The remaining 7500 time steps are used to compute performance measures.

The benchmark uses the LAMMPS (Large-scale Atomic/Molecular Massively Parallel Simulator) code⁴⁶ to run the MD simulations. Consequently, the benchmarked MLP must have LAMMPS bindings.

The benchmark’s `code` contains functionality to

- configure the benchmark, create hydrogen starting configurations, input files, and directory structure (`create_...` routines);
- run MD simulations (`run_simulations` routine);
- extract information and MD-derived properties (`get_...` routines);
- create figures (`figure_...` routines) and tables (`table_...` routines).

The benchmark is written in the open-source programming language Python (Python Software Foundation, python.org). The benchmark repository (Section 8) provides two Jupyter (NumFOCUS Foundation, jupyter.org) notebooks. One demonstrates benchmarking of an MLP and can serve as a starting point; the other generates Figures 3 and SI3 and Tables 1 and 2 in this work.

7 Results and discussion

We benchmark several interatomic potentials of increasing complexity, ranging from traditional empirical potentials to a state-of-the-art message-passing neural network. We selected these potentials for diversity, covering local and semilocal models, different representations of atomic environments, and multiple regression algorithms. Together, these potentials cover the whole range of the trade-off between computational efficiency and predictive accuracy. Specifically, we benchmark the following potentials:

- (a) The two-body Yukawa⁴⁷ and the three-body Tersoff⁴⁸ potential, two established traditional empirical potentials. These are not MLPs but serve as baseline models. Both were reparametrised for the h-11pt-24 dataset. These are the fastest potentials in the selection and have the fewest parameters.
- (b) Ultra-fast potentials³ in a two-body and a three-body parametrisation. These MLPs represent effective two- and three-body terms in a cubic B-spline basis, with coefficients determined via regularised linear regression. They are as fast as traditional empirical potentials but more flexible.
- (c) PACE (performant ACE)⁴⁹ and MACE (multi-ACE)³⁵, two MLPs based on the atomic cluster expansion (ACE),⁵⁰ a complete representation of local atom environments. PACE uses semi-linear regression; MACE is a message-passing neural network with equivariant higher-order messages.

Table 1 presents the main benchmark results. For the MLPs above and the four MD-derived properties of Section 5—pressure p , stable molecular fraction μ , (self)diffusion coefficient D , and RDF g —we report average HDs between reference DFT/PBE (six repetitions) and MLP-accelerated (12 repetitions) MD simulations. Figure 5 shows stable molecular fractions and diffusion coefficients for the UFP2, UFP3, PACE, and MACE MLPs. Property and scatter plots for all MLPs can be found in Figures SI2 and SI3.

The Yukawa and the Tersoff potential fail to reproduce the MD-derived properties. Since the UFP2 and UFP3 potentials perform markedly better, we attribute this failure to the fixed functional forms of the traditional empirical potentials. In the following, we will not discuss the Yukawa and Tersoff potentials further.

UFP3 performs as well as or better than UFP2 for all properties, consistent with its increased fitting capacity from its three-body terms. UFP3 is also the first MLP to start qualitatively capturing the properties of WDH (Figure 5).

PACE improves substantially over UFP3 in HD and visual assessment but does not yet closely match the properties from the reference MD simulations. MACE, in turn, improves substantially over PACE in HD, with the largest improvement in Table 1, and visual assessment. It is the only benchmarked MLP whose MD-derived properties quantitatively agree with the DFT/PBE reference.

Overall, we observe that $\text{HD}(p) > \text{HD}(\mu) > \text{HD}(D) > \text{HD}(g)$ (except for μ and D for the Tersoff potential, which we attribute to noise), indicating that pressures are harder to reproduce than stable molecular fractions than diffusion coefficients than RDFs. The performance of MLPs improves with their complexity (and computational requirements).

MLP	Rank	HDs between MD Properties				
		p	μ	D	g	\emptyset
Yukawa	5.5	1.00	1.00	0.99	0.79	0.95
Tersoff	5.5	1.00	0.95	0.99	0.91	0.96
UFP2	4	1.00	0.87	0.85	0.66	0.85
UFP3	3	0.99	0.88	0.65	0.59	0.78
PACE	2	0.84	0.67	0.60	0.31	0.61
MACE	1	0.27	0.22	0.19	0.10	0.20

Table 1: *Performance comparison* of MLPs. Shown are average HDs for four MD-derived properties (pressure p , stable molecular fraction μ , (self)diffusion coefficient D , RDF g) between properties from DFT reference and MLP-accelerated MD simulations. Best performance in bold.

MLP = machine-learning potential, HD = Hellinger distance, MD = molecular dynamics, DFT = density functional theory.

As an ancillary, Table 2 presents test-set prediction-error statistics. Specifically, it shows MAE, RMSE, and maximum error (max), both as-is and as fractions of their respective ranges, and $\rho = \log(1 - R^2)$, where R is Pearson’s correlation coefficient. For all statistics, lower values are better. For UFP3, PACE, and MACE, the three best-performing MLPs in this benchmark, Figure 6 presents scatter plots of test-set force prediction errors, data distributions, and log-log histograms of prediction errors. For energy and force scatter plots of all MLPs, see Figure SI3.

Test-set prediction errors correlate with performance in MD-derived properties and lead to the same ranking of MLPs. However, from the test-set errors alone, it would have been unclear a priori if and which MLP would lead to property predictions in agreement with the DFT/PBE reference. In particular, the suitability of PACE would have been unclear from test-set errors alone.

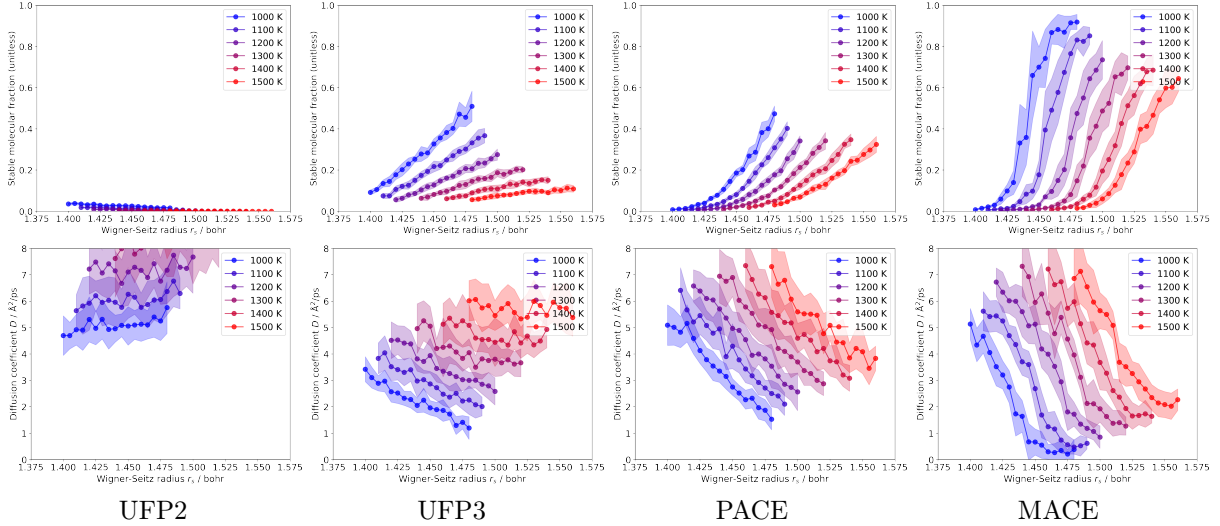


Figure 5: *Derived properties* from MLP-accelerated MD simulations. Shown are stable molecular fractions (top row) and diffusion coefficients (bottom row) for UFP2, UFP3, PACE, and MACE (left to right).

Table 2: *Test-set prediction error* statistics for selected MLPs. Shown are, for energies and forces (component-wise), MAE, RMSE, maximum absolute error (max), both as-is and as a fraction of their respective ranges, as well as $\rho = \log_{10}(1 - R^2)$, where R is Pearson’s correlation coefficient. Best performance in bold.

MLP = machine-learning interatomic potential, MAE = mean absolute error, RMSE = root-mean-squared error.

MLP	E / meV/atom						F / meV/Å			
	MAE %	RMSE %	max %	ρ	MAE %	RMSE %	max %	ρ		
Yukawa	112 4.69	193 8.11	850 36	-0.79	964 0.84	1434 1.25	46 k 40	-0.22		
Tersoff	90 3.76	170 7.11	923 39	-1.78	820 0.72	1485 1.30	55 k 48	-0.23		
UFP2	21 0.88	31 1.30	139 5.83	-2.19	646 0.56	912 0.80	15 k 13	-0.64		
UFP3	8.3 0.35	13 0.55	118 4.96	-3.00	406 0.35	611 0.53	14 k 13	-1.00		
PACE	6.0 0.25	7.5 0.32	30 1.27	-3.46	210 0.18	351 0.31	40 k 35	-1.45		
MACE	1.6 0.07	2.1 0.09	14 0.57	-4.56	86 0.08	129 0.11	8 k 7	-2.31		

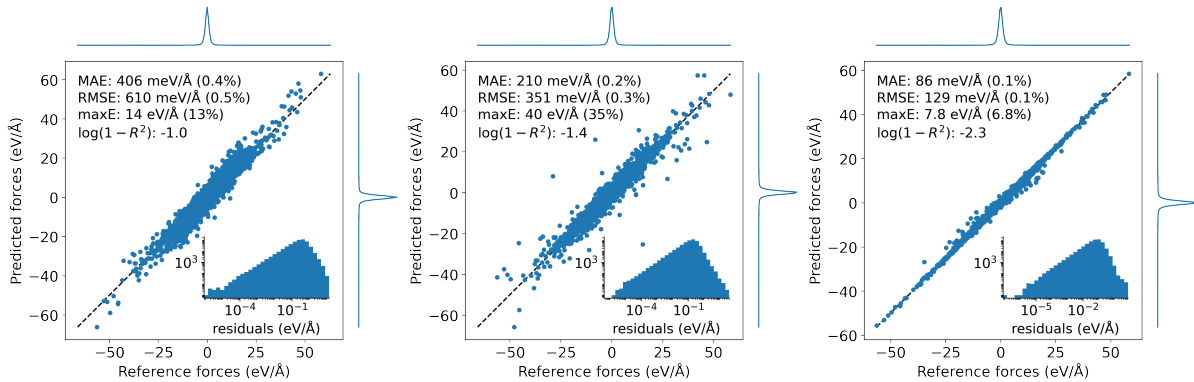


Figure 6: *Test-set prediction errors for forces* (component-wise) of the UFP3 (left), PACE (middle), and MACE (right) MLPs. Shown are predictions versus DFT reference (dots), error statistics (top left inside of plots), data distributions (top and right outside of plots), and a log-log histogram of prediction errors (inset). See Section 5 for details and Figure SI3 for scatter plots of energies and forces for all MLPs.

8 Conclusions

This work provides the automated `h-11pt-24` benchmark for MLPs that characterises their ability to model the physics of the LLPT between atomic and molecular WDH. The benchmark goes beyond test-set error statistics, which do not guarantee physical simulations, yet requires no expert domain knowledge.

The benchmark focuses on an MLP’s ability to learn a complex high-dimensional potential-energy surface. In line with this, the performance ranking of MLPs in Table 1 corresponds to the complexity of the benchmarked MLPs.

A limitation of the benchmark is the restriction to a single MD package. In particular, for experimental, less mature MLPs, a LAMMPS interface might not be available. Hence, supporting another widely used MD package, such as the Atomic Simulation Environment (ASE),⁵¹ would be desirable.

The benchmark could, in principle, be extended to active learning if the computational requirements of the used reference ab-initio method can be limited sufficiently to facilitate benchmarking. For DFT, this could be attempted, e.g., via lower-rung functionals and smaller basis sets.

Other challenging aspects of MLP development that could benefit from future automated application-driven benchmarks include the ability to model many chemical elements, e.g., high-entropy alloys, and the ability to model long-ranged interactions, e.g., van-der-Waals materials.

Acknowledgments

The authors thank Marcel F. Langer, Michele Ceriotti, Richard G. Hennig, Stephen R. Xie, Ajinkya Hire, Hendrik Kraß, Kousuke Nakano, Andrea Tirelli, Giacomo Tenti, Michele Casula, Ralf Drautz, Gábor Csányi for constructive discussions of the benchmark, WDH, and specific MLPs.

This project has received funding from the European Union’s Horizon 2020 research and innovation programme under Grant Agreement No. 952165, European Center of Excellence in Exascale Computing TREX, Targeting Real chemical accuracy at the Exascale. Calculations were performed at the bwUni-Cluster 2.0 as part of the high-performance-computing infrastructure of the state of Baden-Württemberg.

Data and code availability

The benchmark code and `h-11pt-24` dataset are available at <https://gitlab.com/qmml/h-benchmark> under the Apache license 2.0. The raw data underlying the `h-11pt-24` dataset are available at <https://zenodo.org/deposit/8160491>.

References

1. Oliver T. Unke, Stefan Chmiela, Huziel E. Sauceda, Michael Gastegger, Igor Poltavsky, Kristof T. Schütt, Alexandre Tkatchenko, Klaus-Robert Müller: *Machine learning force fields*. Chemical Reviews 121(16): 10142, 2021.
2. Yunxing Zuo, Chi Chen, Xiangguo Li, Zhi Deng, Yiming Chen, Jörg Behler, Gábor Csányi, Alexander V. Shapeev, Aidan P. Thompson, Mitchell A. Wood, et al.: *Performance and cost assessment of machine learning interatomic potentials*. The Journal of Physical Chemistry A 124(4): 731, 2020.
3. Stephen R. Xie, Matthias Rupp, Richard G. Hennig: *Ultra-fast interpretable machine-learning potentials*. npj Computational Materials 9: 162, 2023.
4. Jeffrey Li, Chen Qu, Joel M. Bowman: *Diffusion Monte Carlo with fictitious masses finds holes in potential energy surfaces*. Molecular Physics 119(17–18): e1976426, 2021.
5. Sina Stocker, Johannes Gasteiger, Florian Becker, Stephan Günnemann, Johannes T. Margraf: *How robust are modern graph neural network potentials in long and hot molecular dynamics simulations?* Machine Learning: Science and Technology 3(4): 045010, 2022.
6. Xiang Fu, Zhenghao Wu, Wujie Wang, Tian Xie, Sinan Keten, Rafael Gomez-Bombarelli, Tommi Jaakkola: *Forces are not enough: Benchmark and critical evaluation for machine learning force fields with molecular simulations*. Transactions on Machine Learning Research 798, 2023.

7. Joe D. Morrow, John L. A. Gardner, Volker L. Deringer: *How to validate machine-learned interatomic potentials*. The Journal of Chemical Physics 158(12): 121501, 2023.
8. Matthias Rupp, Alexandre Tkatchenko, Klaus-Robert Müller, O. Anatole von Lilienfeld: *Fast and accurate modeling of molecular atomization energies with machine learning*. Physical Review Letters 108(5): 058301, 2012.
9. Michael Bonitz, Jan Vorberger, Mandy Bethkenhagen, Maximilian Böhme, David Ceperley, Alexey Filinov, Thomas Gawne, Frank Graziani, Gianluca Gregori, Paul Hamann, et al.: *First principles simulations of dense hydrogen*. arXiv 2405.10627, 2024.
10. Ravit Helled, Guglielmo Mazzola, Ronald Redmer: *Understanding dense hydrogen at planetary conditions*. Nature Reviews Physics 2(10): 562, 2020.
11. Katerina Falk: *Experimental methods for warm dense matter research*. High Power Laser Science and Engineering 6: e59, 2018.
12. Hua Y. Geng, Q. Wu, Miriam Marqués, Graeme J. Ackland: *Thermodynamic anomalies and three distinct liquid-liquid transitions in warm dense liquid hydrogen*. Physical Review B 100(13): 134109, 2019.
13. John P. Perdew, Kieron Burke, Matthias Ernzerhof: *Generalized gradient approximation made simple*. Physical Review Letters 77(18): 3865, 1996.
14. Bingqing Cheng, Guglielmo Mazzola, Chris J. Pickard, Michele Ceriotti: *Evidence for supercritical behaviour of high-pressure liquid hydrogen*. Nature 585(7824): 217, 2020.
15. Valentin V. Karasiev, Joshua Hinz, Suxing Hu, Samuel B. Trickey: *On the liquid-liquid phase transition of dense hydrogen*. Nature 600(7889): E12, 2021.
16. Bingqing Cheng, Guglielmo Mazzola, Chris J. Pickard, Michele Ceriotti: *Reply to: On the liquid-liquid phase transition of dense hydrogen*. Nature 600(7889): E15, 2021.
17. Sandro Scandolo: *Liquid-liquid phase transition in compressed hydrogen from first-principles simulations*. Proceedings of the National Academy of Sciences of the United States of America 100(6): 3051, 2003.
18. Miguel A. Morales, Carlo Pierleoni, Eric Schwegler, David M. Ceperley: *Evidence for a first-order liquid-liquid transition in high-pressure hydrogen from ab initio simulations*. Proceedings of the National Academy of Sciences of the United States of America 107(29): 12799, 2010.
19. Winfried Lorenzen, Bastian Holst, Ronald Redmer: *First-order liquid-liquid phase transition in dense hydrogen*. Physical Review B 82(19): 195107, 2010.
20. Jan Vorberger, Isaac Tamblyn, Burkhard Militzer, Stanimir A. Bonev: *Hydrogen-helium mixtures in the interiors of giant planets*. Physical Review B 75(2): 024206, 2007.
21. Kris T. Delaney, Carlo Pierleoni, David M. Ceperley: *Quantum Monte Carlo simulation of the high-pressure molecular-atomic crossover in fluid hydrogen*. Physical Review Letters 97(23): 235702, 2006.
22. Guglielmo Mazzola, Ravit Helled, Sandro Sorella: *Phase diagram of hydrogen and a hydrogen-helium mixture at planetary conditions by quantum Monte Carlo simulations*. Physical Review Letters 120(2): 025701, 2018.
23. Mark E. Tuckerman: *Statistical Mechanics: Theory and Molecular Simulation*. 2nd edition. Oxford University Press, 2023.
24. Johannes Hoja, Leonardo Medrano Sandonas, Brian G. Ernst, Alvaro Vazquez-Mayagoitia, Robert A. DiStasio, Jr., Alexandre Tkatchenko: *QM7-X, a comprehensive dataset of quantum-mechanical properties spanning the chemical space of small organic molecules*. Scientific Data 8: 43, 2021.
25. Raghunathan Ramakrishnan, Pavlo O. Dral, Matthias Rupp, O. Anatole von Lilienfeld: *Quantum chemistry structures and properties of 134 kilo molecules*. Scientific Data 1: 140022, 2014.
26. Stefan Chmiela, Alexandre Tkatchenko, Huziel E. Sauceda, Igor Poltavsky, Kristof T. Schütt, Klaus-Robert Müller: *Machine learning of accurate energy-conserving molecular force fields*. Science Advances 3(5): e1603015, 2017.

27. Anders S. Christensen, O. Anatole von Lilienfeld: *On the role of gradients for machine learning of molecular energies and forces*. Machine Learning: Science and Technology 1(4): 045018, 2020.
28. Lowik Chanussot, Abhishek Das, Siddharth Goyal, Thibaut Lavril, Muhammed Shuaibi, Morgane Riviere, Kevin Tran, Javier Heras-Domingo, Caleb Ho, Weihua Hu, et al.: *Open Catalyst 2020 (OC20) dataset and community challenges*. ACS Catalysis 11(10): 6059, 2021.
29. Lowik Chanussot, Abhishek Das, Siddharth Goyal, Thibaut Lavril, Muhammed Shuaibi, Morgane Riviere, Kevin Tran, Javier Heras-Domingo, Caleb Ho, Weihua Hu, et al.: *Correction to “The Open Catalyst 2020 (OC20) dataset and community challenges”*. ACS Catalysis 11(21): 13062, 2021.
30. Joshua A. Vita, Eric G. Fuemmeler, Amit Gupta, Gregory P. Wolfe, Alexander Quanming Tao, Ryan S. Elliott, Stefano Martiniani, Ellad B. Tadmor: *ColabFit exchange: Open-access datasets for data-driven interatomic potentials*. The Journal of Chemical Physics 159(15): 154802, 2023.
31. Johannes Gasteiger, Florian Becker, Stephan Günnemann: *GemNet: Universal directional graph neural networks for molecules*. In *Advances in Neural Information Processing Systems (NeurIPS), Virtual, December 6–14, 2021*.
32. Xiang Fu, Zhenghao Wu, Wujie Wang, Tian Xie, Sinan Keten, Rafael Gomez-Bombarelli, Tommi Jaakkola: *Benchmarking ML for MD simulation*. Code repository at github.com/kyonofx/MDsim. Accessed 2024-08-08.
33. Gregory Fonseca, Igor Poltavsky, Alexandre Tkatchenko: *Force field analysis software and tools (FFAST): Assessing machine learning force fields under the microscope*. Journal of Chemical Theory and Computation 19(23): 8706, 2023.
34. Simon Batzner, Albert Musaelian, Lixin Sun, Mario Geiger, Jonathan P. Mailoa, Mordechai Kornbluth, Nicola Molinari, Tess E. Smidt, Boris Kozinsky: *E(3)-equivariant graph neural networks for data-efficient and accurate interatomic potentials*. Nature Communications 13: 2453, 2022.
35. Ilyes Batatia, Dávid Péter Kovács, Gregor N. C. Simm, Christoph Ortner, Gábor Csányi: *MACE: Higher order equivariant message passing neural networks for fast and accurate force fields*. In Sanmi Koyejo, Shaker Mohamed, Alekh Agarwal, Danielle Belgrave, Kyunghyun Cho, Alice H. Oh (editors), *NeurIPS Proceedings*, 11 423–11 436. Curran Assoc., 2022.
36. Burr Settles: *Active Learning*, volume 18 of *Synthesis Lectures on Artificial Intelligence and Machine Learning*. Morgan & Claypool, 2012.
37. Gábor Csányi, Tristan Albaret, Mike C. Payne, Alessandro De Vita: *“Learn on the fly”: A hybrid classical and quantum-mechanical molecular dynamics simulation*. Physical Review Letters 93(17): 175503, 2004.
38. Paolo Giannozzi, Stefano Baroni, Nicola Bonini, Matteo Calandra, Roberto Car, Carlo Cavazzoni, Davide Ceresoli, Guido L. Chiarotti, Matteo Cococcioni, Ismaila Dabo, et al.: *QUANTUM ESPRESSO: a modular and open-source software project for quantum simulations of materials*. Journal of Physics: Condensed Matter 21(39): 395502, 2009.
39. Paolo Giannozzi, Oliviero Andreussi, Thomas Brumme, Oana Bunau, Marco Buongiorno Nardelli, Matteo Calandra, Roberto Car, Carlo Cavazzoni, Davide Ceresoli, Matteo Cococcioni, et al.: *Advanced capabilities for materials modelling with Quantum ESPRESSO*. Journal of Physics: Condensed Matter 29(46): 465901, 2017.
40. Joshua Hinz, Valentin V. Karasiev, Su Xing Hu, Mohamed Zaghoo, Daniel Mejía-Rodríguez, Samuel B. Trickey, Lucas Calderín: *Fully consistent density functional theory determination of the insulator-metal transition boundary in warm dense hydrogen*. Physical Review Research 2(3): 032065(R), 2020.
41. Andrea Tirelli, Giacomo Tenti, Kousuke Nakano, Sandro Sorella: *High-pressure hydrogen by machine learning and quantum Monte Carlo*. Physical Review B 106(4): L041105, 2022.
42. Hongwei Niu, Yubo Yang, Scott Jensen, Markus Holzmann, Carlo Pierleoni, David M. Ceperley: *Stable solid molecular hydrogen above 900 K from a machine-learned potential trained with diffusion quantum Monte Carlo*. Physical Review Letters 130(7): 076102, 2023.

43. Edward J. Maginn, Richard A. Messerly, Daniel J. Carlson, Daniel R. Roe, J. Richard Elliot: *Best practices for computing transport properties 1. Self-diffusivity and viscosity from equilibrium molecular dynamics [article v1.0]*. Living Journal of Computational Molecular Science 1(1): 6324, 2020.
44. Ernst Hellinger: *Neue Begründung der Theorie quadratischer Formen von unendlich vielen Veränderlichen*. Journal für die reine und angewandte Mathematik 1909(136): 210, 1909.
45. Anil Bhattacharyya: *On a measure of divergence between two multinomial populations*. Sankhyā: The Indian Journal of Statistics 7(4): 401, 1946.
46. Aidan P. Thompson, H. Metin Aktulga, Richard Berger, Dan S. Bolintineanu, Miachel W. Brown, Paul S. Crozier, Pieter J. in't Veld, Axel Kohlmeyer, Stan G. Moore, Trung Dac Nguyen, et al.: *LAMMPS—a flexible simulation tool for particle-based materials modeling at the atomic, meso, and continuum scales*. Computer Physics Communications 271: 108171, 2022.
47. Hideki Yukawa: *On the interaction of elementary particles. I*. Proceedings of the Physico-Mathematical Society of Japan 17: 48, 1935.
48. Jerry Tersoff: *Empirical interatomic potential for silicon with improved elastic properties*. Physical Review B 38(14): 9902, 1988.
49. Yury Lysogorskiy, Cas van der Oord, Anton Bochkarev, Sarath Menon, Matteo Rinaldi, Thomas Hammerschmidt, Matous Mrovec, Aidan P. Thompson, Gábor Csányi, Christoph Ortner, et al.: *Performant implementation of the atomic cluster expansion (PACE) and application to copper and silicon*. npj Computational Materials 7: 97, 2021.
50. Ralf Drautz: *Atomic cluster expansion for accurate and transferable interatomic potentials*. Physical Review B 99(1): 249901, 2019.
51. Ask Hjorth Larsen, Jens Jørgen Mortensen, Jakob Blomqvist, Ivano E. Castelli, Rune Christensen, Marcin Dułak, Jesper Friis, Michael N. Groves, Bjørk Hammer, Cory Hargus, et al.: *The atomic simulation environment—a Python library for working with atoms*. Journal of Physics: Condensed Matter 29(27): 273002, 2017.

Supplementary Information:

Hydrogen under Pressure as a Benchmark for Machine-Learning Interatomic Potentials

Thomas Bischoff,¹ Bastian Jäckl,¹ Matthias Rupp²

¹ Department of Computer and Information Science, University of Konstanz, Konstanz, Germany

² Luxembourg Institute of Science and Technology (LIST), Esch-sur-Alzette, Luxembourg

A Computational details

A.1 Molecular dynamics simulations

For the reference MD simulations, DFT calculations were carried out using the **Quantum-Espresso**¹ software. We used the semilocal PBE² functional together with a scalar-relativistic, ultrasoft projector-augmented wave (PAW) pseudopotential³ for hydrogen. We set the energy cutoff for the plane-wave basis to 60 Ry and used a shifted $4 \times 4 \times 4$ \mathbf{k} -point sampling. We smeared the occupations of the Kohn-Sham levels⁴ according to the Fermi-Dirac distribution consistent with the ionic temperature applied in the MD simulations. We verified that the employed numerical parameters are consistent with those in the literature⁵⁻⁸.

All MD simulations used cubic supercells. We determined the cubic lattice constant a for each calculation according to the definition of the Wigner-Seitz radius r_s . Specifically, we set $a = (4\pi r_s^3 N/3)^{1/3}$, where $N = 128$ is the number of hydrogen atoms in the unit cell. We verified that 128 hydrogen atoms are sufficient to identify the LLPT, in agreement with the literature.^{5;7;9}

MD simulations were carried out using the **LAMMPS**¹⁰ software in the canonical ensemble (NVT). We set the time step to 0.2 fs and controlled the temperature via a Bussi-Parrinello thermostat¹¹. The time duration of each MD simulation was one ps, of which the first 0.5 ps were used for equilibration, and the remaining 0.5 ps were used for computing the thermodynamic quantities of interest.

We verified that this simulation length is sufficient to obtain converged results for purely atomic or purely molecular hydrogen. In proximity to the LLPT, we observed non-periodic oscillations between the two phases. To ensure sufficient thermodynamic averaging for these cases, we performed six independent MD simulations (of the same duration) for each point in the investigated (T, r_s) phase space (Figure 1).

Individual MD simulations were initialised with distinct starting configurations composed of random atomic coordinates and velocities. The average and standard deviation over the six MD simulations were then considered as the value and statistical uncertainty of the MD-derived properties.

Discarding equilibration, the average over six 0.5 ps MD simulations is equivalent to the average over one three ps MD simulation. However, in the former approach the MD simulations can be run in parallel. In addition, the six uncorrelated starting configurations prevent the hydrogen system from overproportionally remaining in either the atomic or the molecular phase.

The benchmark employs DFT with the PBE functional and classically described nuclei to simulate hydrogen. Such simulations provide a suitable description of the LLPT of WDH.^{5-9;12-15} However, other electronic-structure methods, such as the local density approximation, the strongly constrained and appropriately normed (SCAN)¹⁶ functional, or quantum Monte Carlo approaches, yield quantitatively different descriptions of the LLPT^{5;7;15}. The same holds for neglecting or incorporating the quantum-mechanical nature of the proton.^{8;13;15} Such effects from the choice of electronic-structure method, while important to better understand the physics of the LLPT in WDH, are not relevant for this benchmark, whose sole purpose is to assess the ability of MLPs to reproduce results from a given ground-truth electronic-structure method.

The MLP-accelerated MD simulations follow the DFT MD simulations as closely as possible. They are also carried out using the LAMMPS software and use the same time step, simulation length, equilibration phase, and thermostat. However, enabled by the MLPs computational efficiency, the benchmark runs twelve repetitions for each combination of temperature and Wigner-Seitz radius.

A.2 Molecular dynamics-derived properties and post-processing

Figure SI1 shows the influence of parameter choices on calculated stable molecular fractions μ . Neither the spatial cutoff nor the temporal cutoff qualitatively change the isothermal μ over r_s curves.

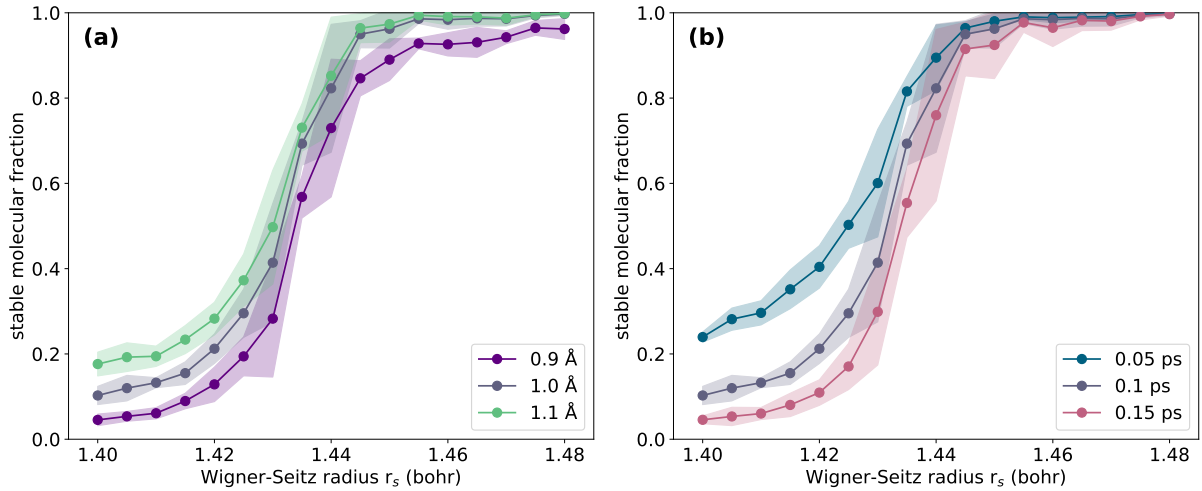


Figure SI1: *Sensitivity of stable molecular fractions to parameter choices.* Shown are stable molecular fractions as a function of cell density for different choices of spatial (left) and temporal cutoff (right).

A.3 Training of machine learning interatomic potentials

The **Yukawa** and **Tersoff** traditional empirical potentials were optimised using the Nelder-Mead simplex algorithm¹⁷ as implemented in the SciPy¹⁸ package. The MD simulations were performed with the standard implementations of these potentials in LAMMPS.

Ultra-fast potentials (UFP2, UFP3) were trained with the Python code available at <https://github.com/uf3/uf3>. For two-body terms, we used a radial cutoff of 3.5 Å and six knots/Å; for three-body terms, we used a cutoff of 2 Å and four knots/Å. The behaviour at the limits of the knot intervals we defined by setting the parameters `leading_trim=0` and `trailing_trim=3`. The energy/force weighting parameter we set to 0.25. For regularisation, we set `ridge_1b=1e-5`, `curvature_1b=0`, `ridge_2b=1e-6`, `curvature_2b=1e-5`, `ridge_3b=1e-6`, and `curvature_3b=1e-8`. The MD simulations were performed with the ML-UF3 plugin for LAMMPS, available at https://github.com/monk-04/uf3/tree/lammps_implementation/lammps_plugin.

PACE was trained using the PACEmaker code^{19;20} documented at <https://pacemaker.readthedocs.io> using the settings below. The MD simulations were performed with the ML-PACE plugin for LAMMPS, available at <https://github.com/ICAMS/lammps-user-pace>.

```

potential:
  deltaSplineBins: 0.001
  elements: [H]
  embeddings:
    ALL: {
      npot: 'FinnisSinclairShiftedScaled',
      fs_parameters: [ 1, 1, 1, 0.5],
      ndensity: 2
    }
  bonds:
    ALL: {
      radbase: ChebExpCos,
      radparameters: [ 5.25 ],
      rcut: 3.0,
      dcut: 0.01,
      NameOfCutoffFunction: cos,
    }
  functions:
    ALL: {
      nradmax_by_orders: [150,20,4,2,2],
      lmax_by_orders: [ 0,5,3,2,2],
    }
}

cutoff: 3.0
seed: 7

fit:
  loss:
    kappa: 0.001
    L1_coeffs: 0.00
    L2_coeffs: 0.00
    w1_coeffs: 0
    w2_coeffs: 0
    w0_rad: 0
    w1_rad: 0
    w2_rad: 0
    optimizer: BFGS
    maxiter: 10000
    fit_cycles: 2

backend:
  evaluator: tensorpot
  batch_size: 50

```

MACE was trained using the ACESuit code available at <https://github.com/ACESuit/mace>, using the command string

```

python ./mace/scripts/run_train.py -name="ScaleShiftMACE" -model=MACE
-train_file="train.xyz" -valid_fraction=0.05 -test_file="test.xyz"
-EOs='1:-13.663181292231226' -model="ScaleShiftMACE"
-hidden_irreps='128x0e + 128x1o + 128x2e' -r_max=3.5 -batch_size=8
-max_num_epochs=80 -ema -ema_decay=0.99 -amsgrad -default_dtype="float64"
-device=cuda -seed=1 -swa

```

The MD simulations were performed with the MACE plugin for LAMMPS described at <https://mace-docs.readthedocs.io>, section "MACE in LAMMPS".

B Analysis details

B.1 Derived properties

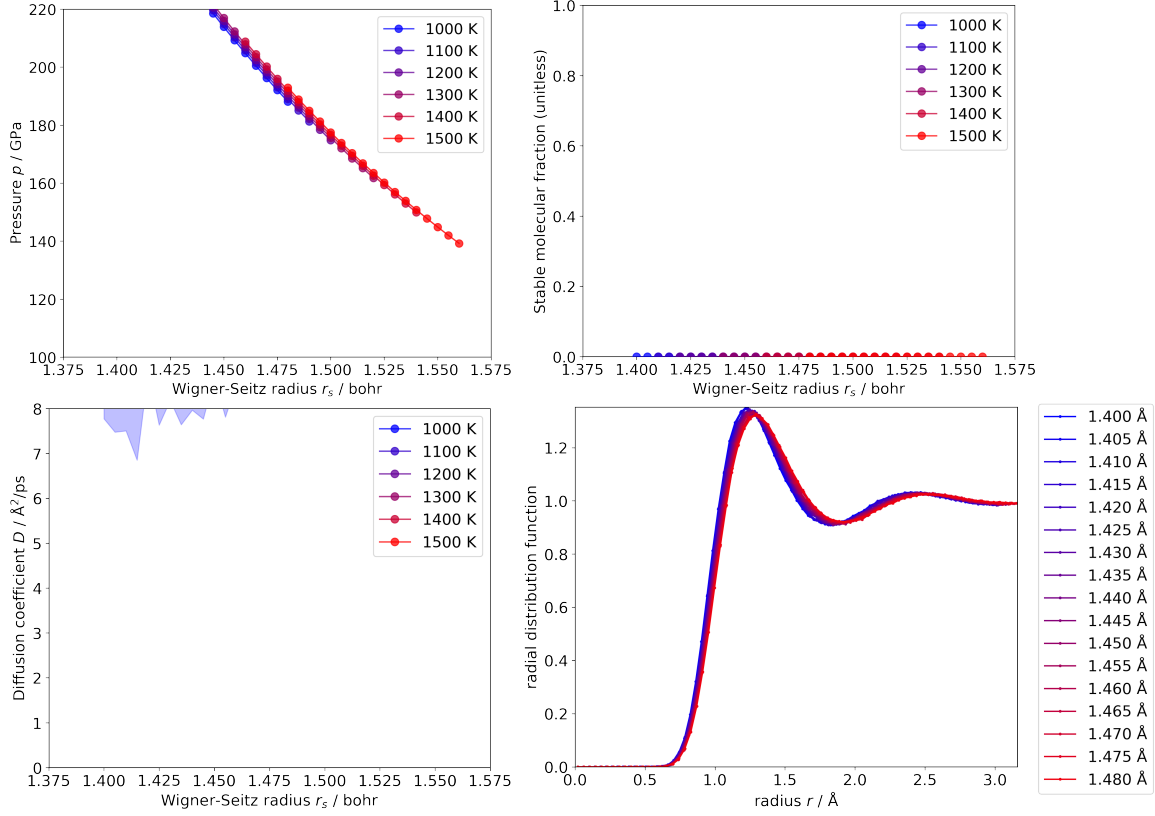
Figure SI2 presents MD-derived properties for all benchmarked MLPs.

B.2 Scatter plots

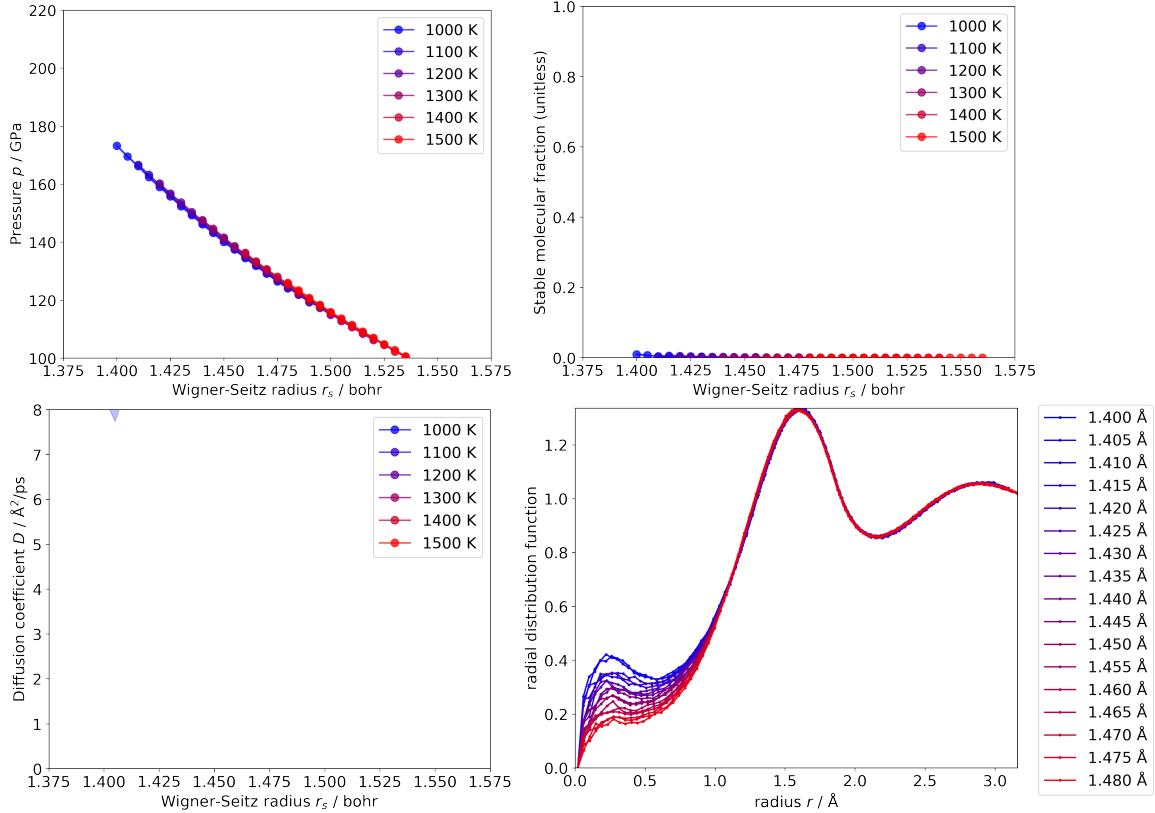
Figure SI3 presents scatter plots showing test-set predictions for all benchmarked MLPs.

B.3 Hellinger distances

Table SI2 presents HDs for all MD-derived properties for all benchmarked MLPs. Wigner-Seitz radii are given as indices, specified by Table SI1.

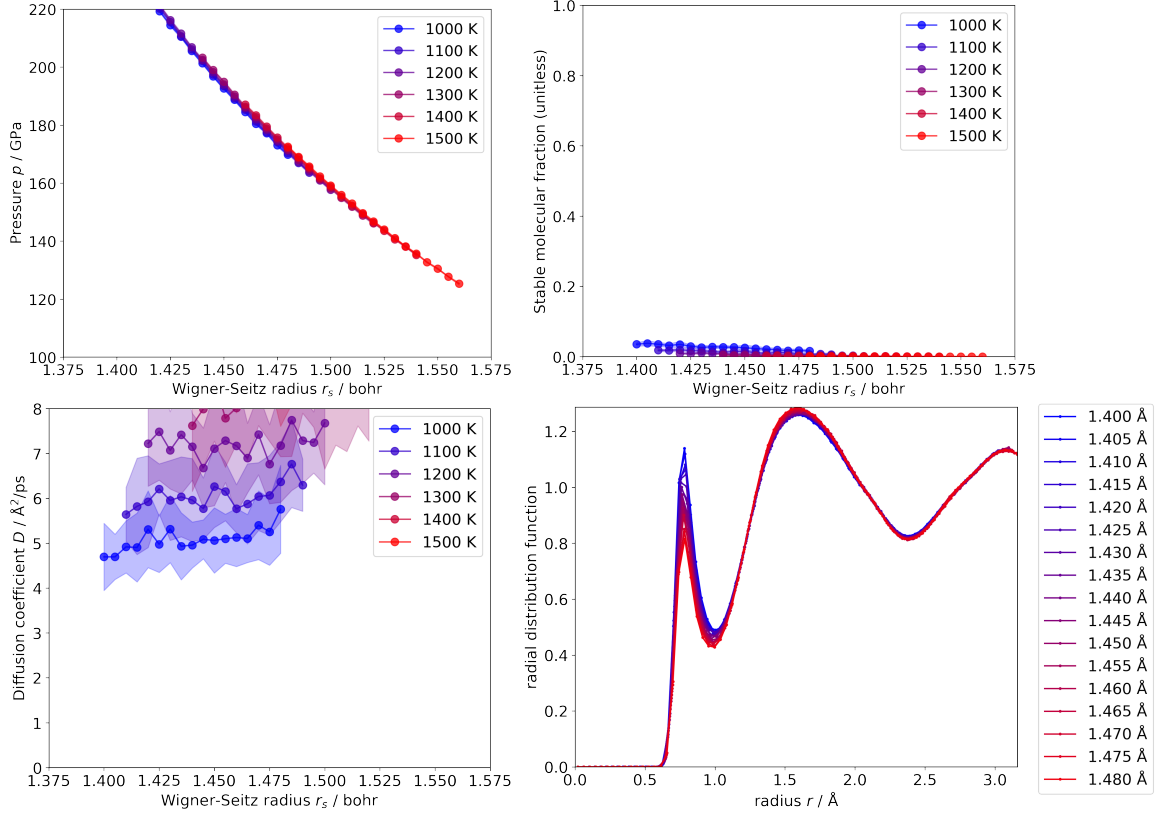


(a) Yukawa potential.

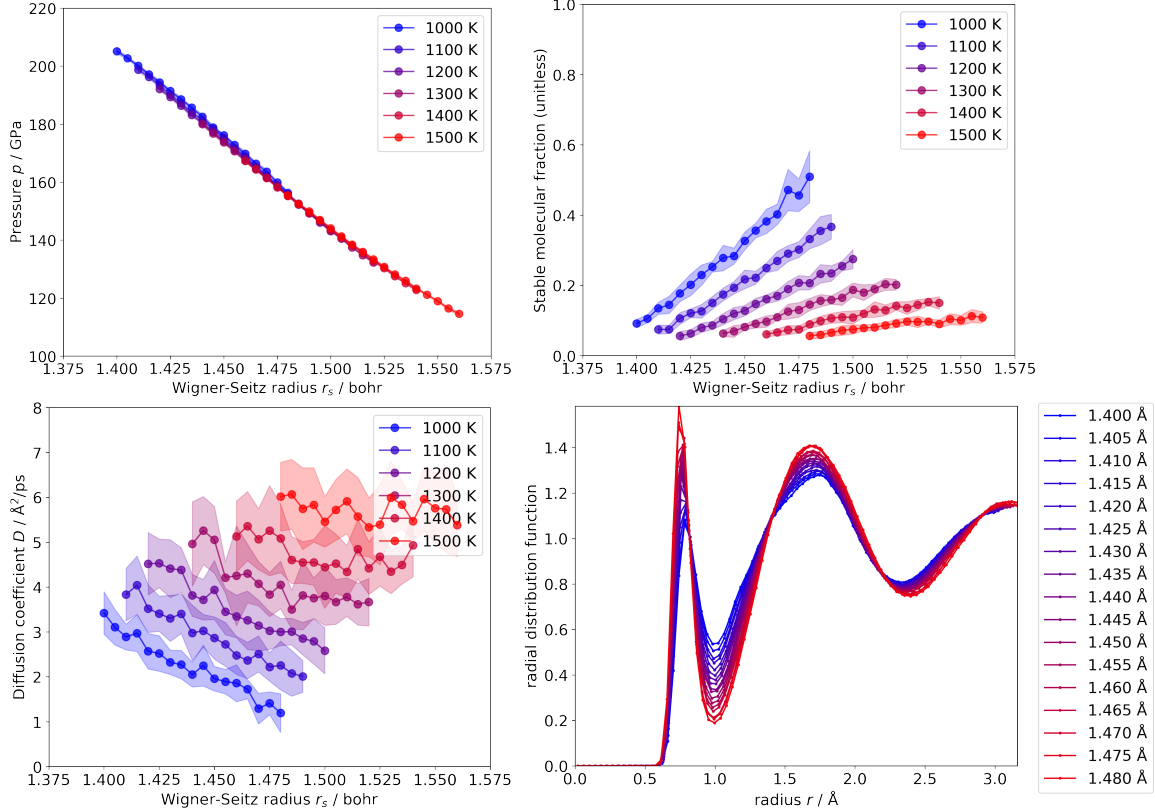


(b) Tersoff potential.

Figure SI2: *Derived properties*. Shown are pressure (top left), stable molecular fraction (top right), and diffusion coefficient (bottom left) as a function of the Wigner-Seitz radius r_s and for different temperatures (color-coded), as well as radial distribution functions (bottom right) at 1000 K for different Wigner-Seitz radii (color-coded), for all benchmarked MLPs (a–f). See Section 5 for details.

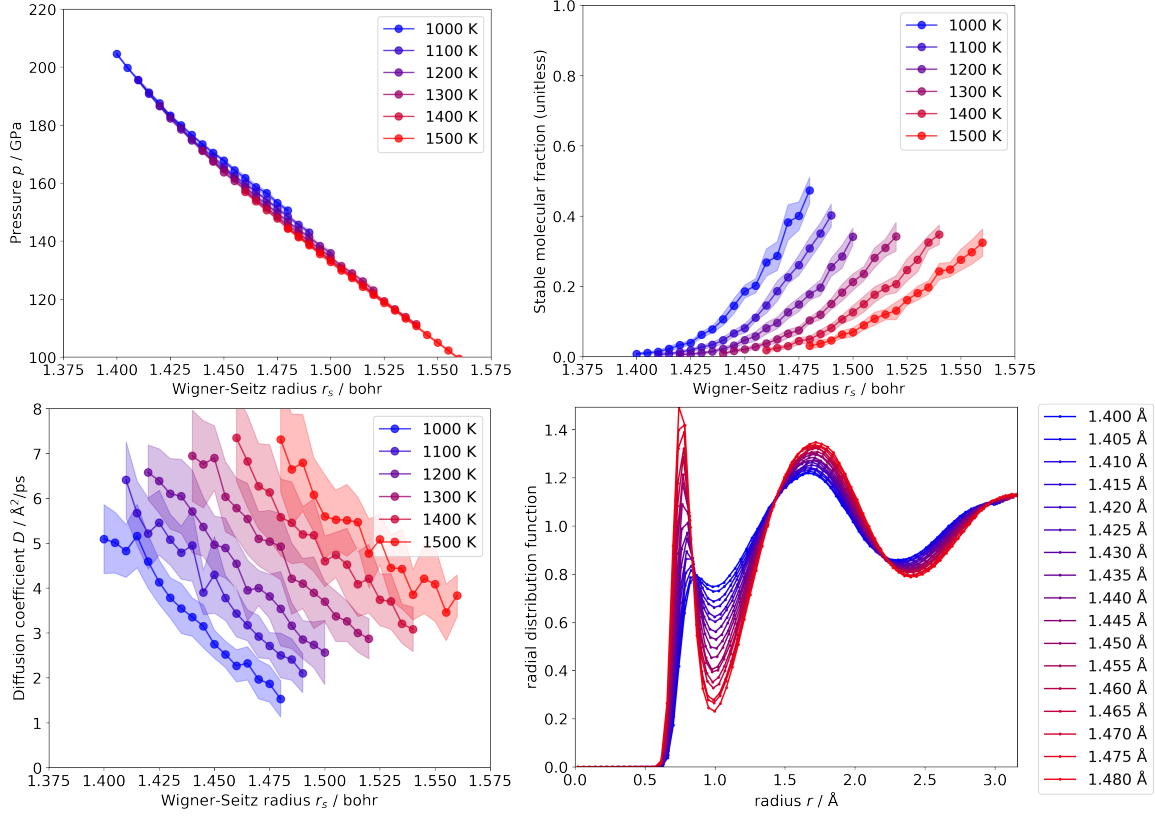


(c) UFP2 potential.

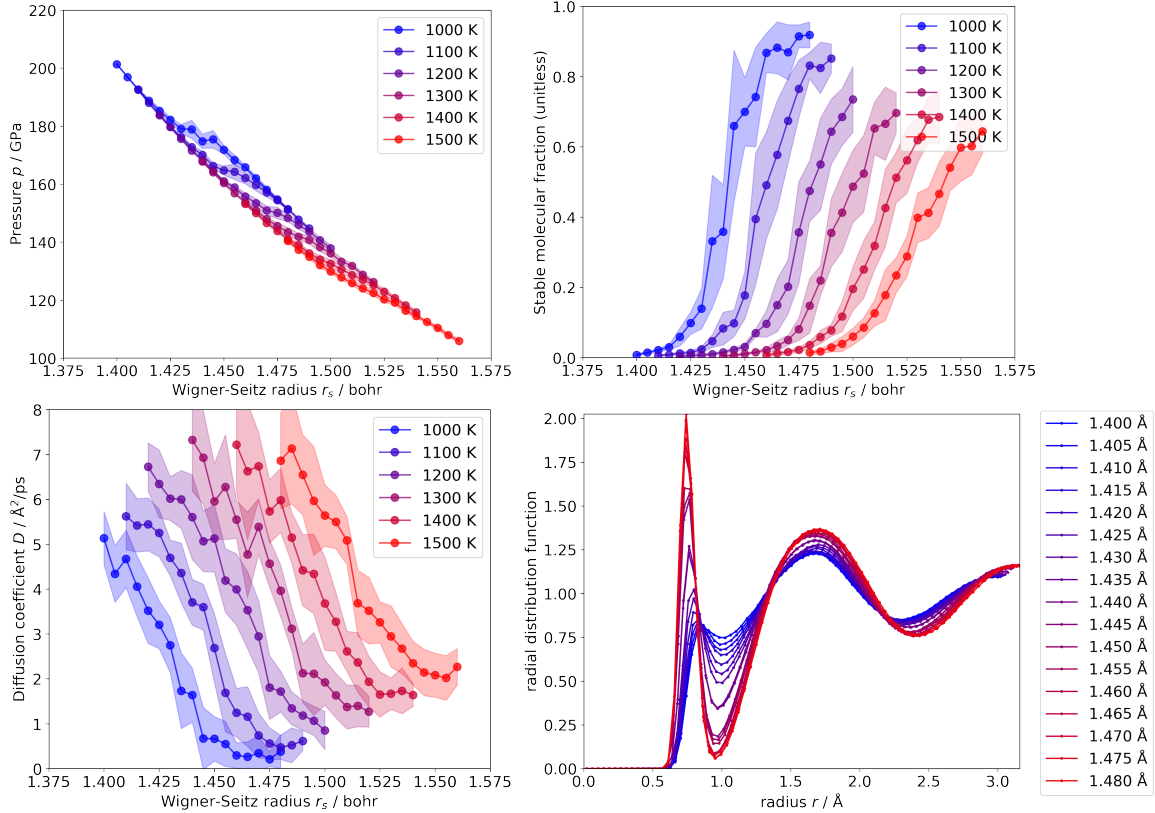


(d) UFP3 potential.

Figure SI2: *Derived properties* (continued). Shown are pressure (top left), stable molecular fraction (top right), and diffusion coefficient (bottom left) as a function of the Wigner-Seitz radius r_s and for different temperatures (color-coded), as well as radial distribution functions (bottom right) at 1000 K for different Wigner-Seitz radii (color-coded), for all benchmarked MLPs (a–f). See Section 5 for details.

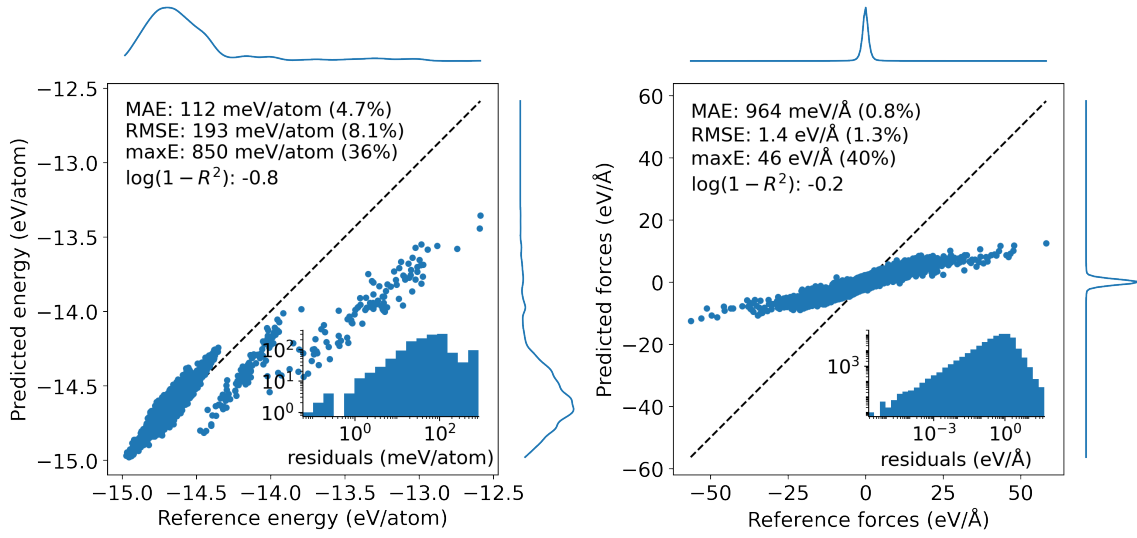


(e) PACE potential.

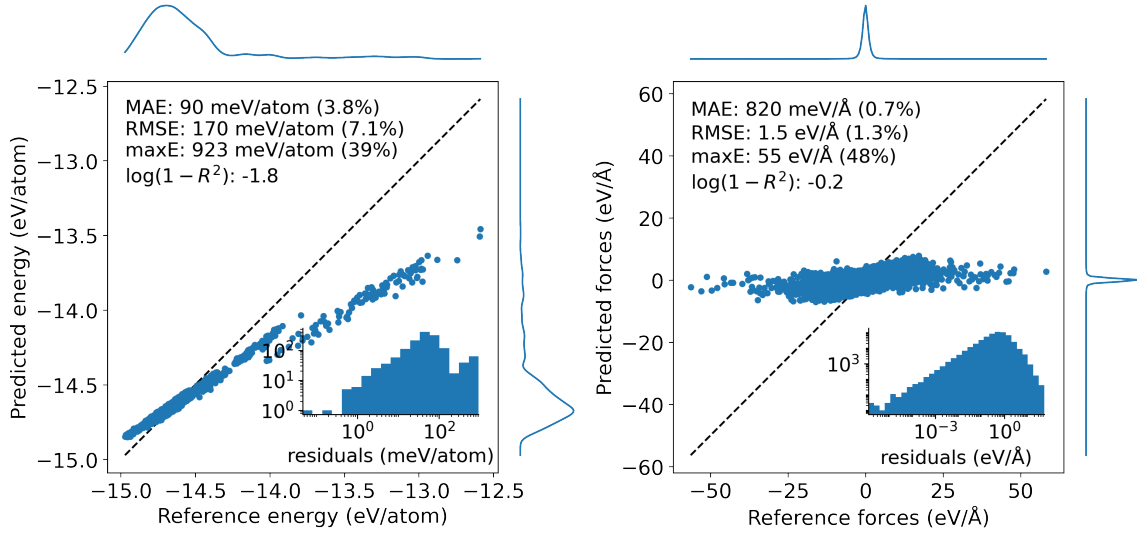


(f) MACE potential.

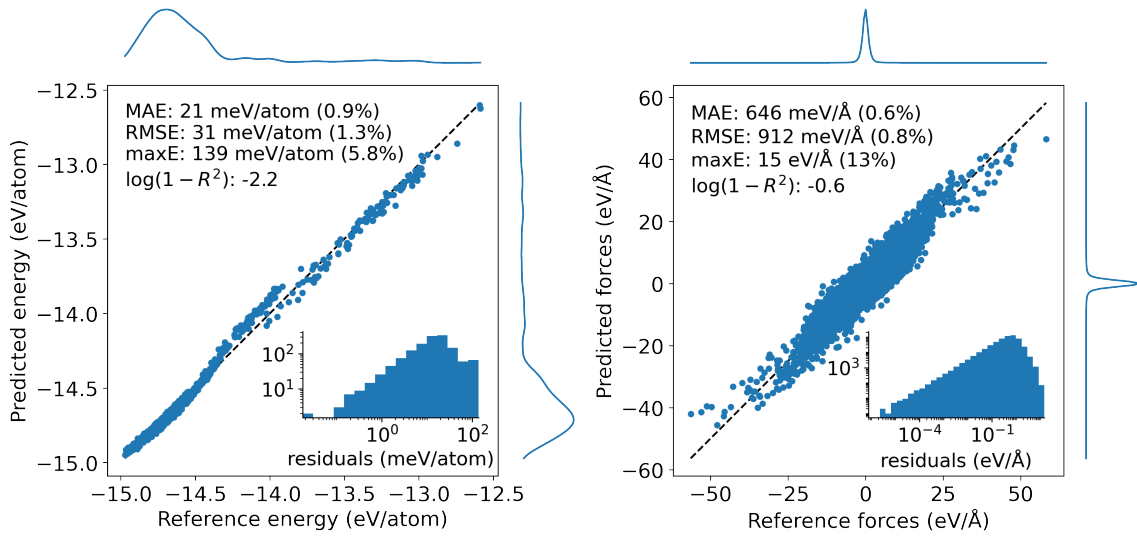
Figure SI2: *Derived properties* (continued). Shown are pressure (top left), stable molecular fraction (top right), and diffusion coefficient (bottom left) as a function of the Wigner-Seitz radius r_s and for different temperatures (color-coded), as well as radial distribution functions (bottom right) at 1000 K for different Wigner-Seitz radii (color-coded), for all benchmarked MLPs (a–f). See Section 5 for details.



(a) Yukawa potential.

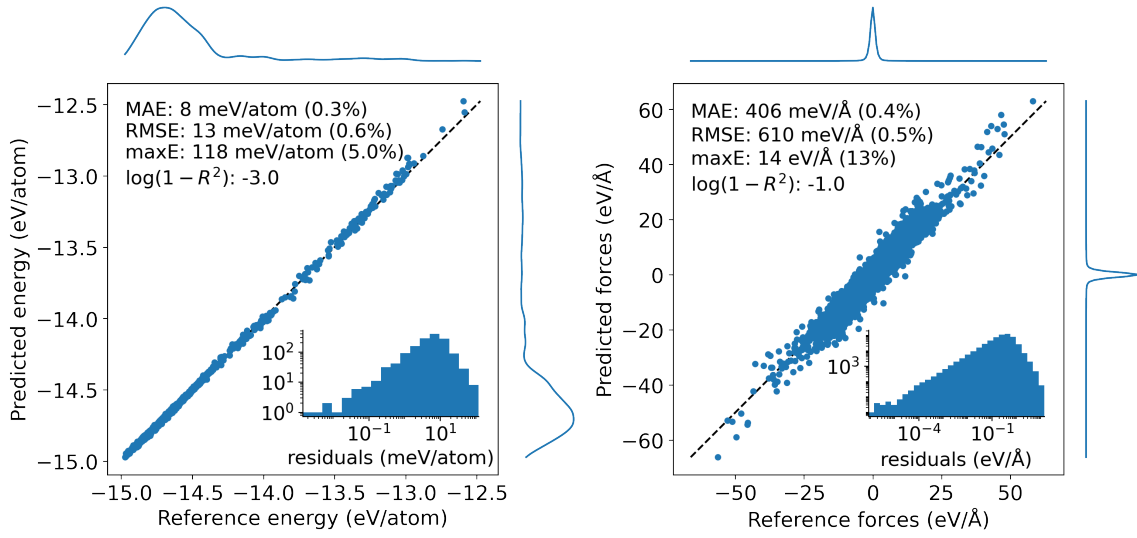


(b) Tersoff potential.

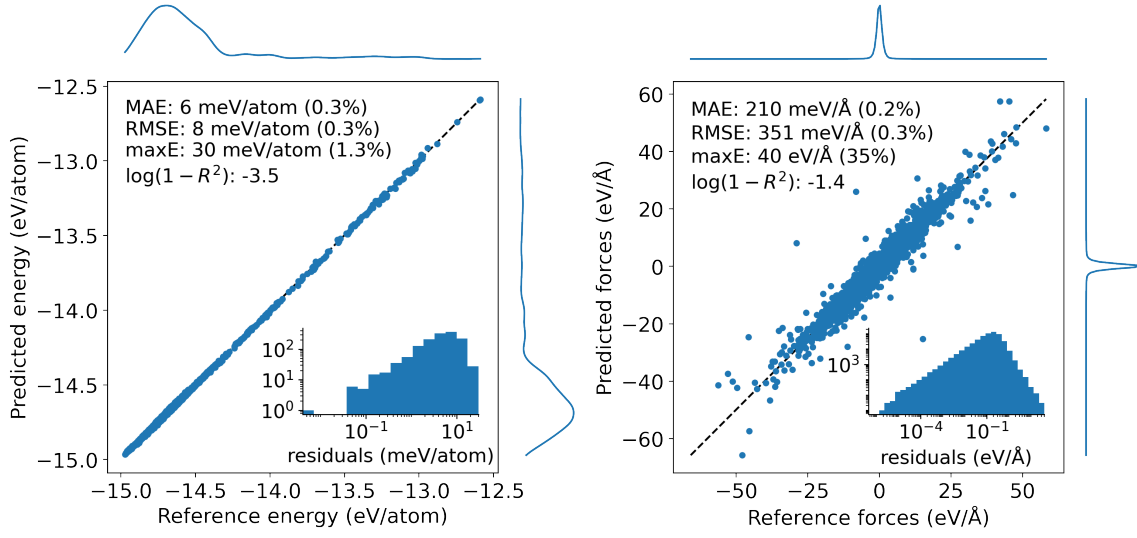


(c) UFP2 potential.

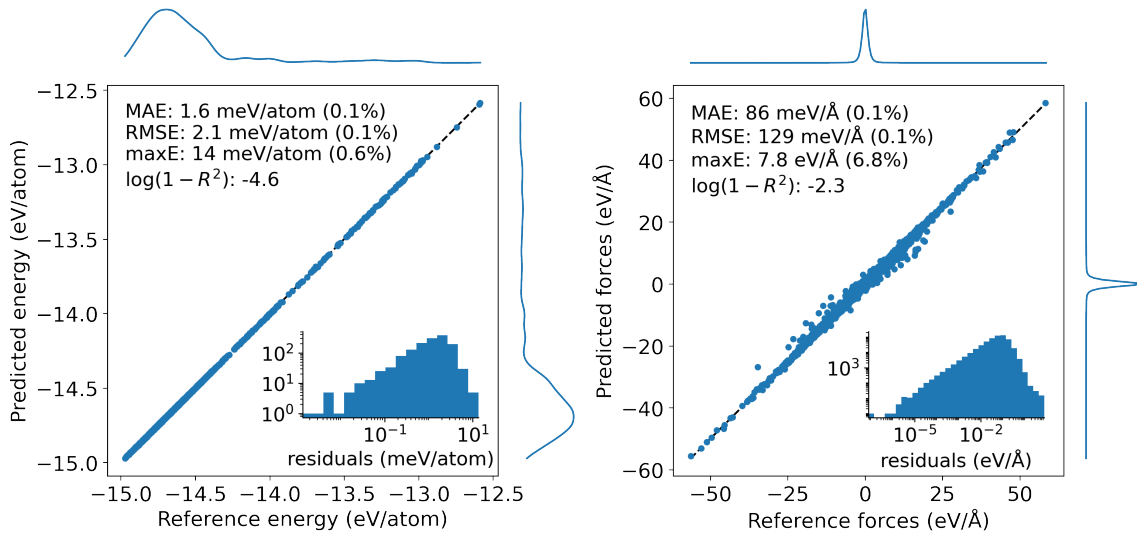
Figure S13: *Scatter plots*. See main text for explanation.



(d) UFP3 potential.



(e) PACE potential.



(f) MACE potential.

Figure SI3: *Scatter plots* (continued). See main text for explanation.

I.	Temperature / K					
	1000	1100	1200	1300	1400	1500
1	1.400	1.410	1.420	1.440	1.460	1.480
2	1.405	1.415	1.425	1.445	1.465	1.485
3	1.410	1.420	1.430	1.450	1.470	1.490
4	1.415	1.425	1.435	1.455	1.475	1.495
5	1.420	1.430	1.440	1.460	1.480	1.500
6	1.425	1.435	1.445	1.465	1.485	1.505
7	1.430	1.440	1.450	1.470	1.490	1.510
8	1.435	1.445	1.455	1.475	1.495	1.515
9	1.440	1.450	1.460	1.480	1.500	1.520
10	1.445	1.455	1.465	1.485	1.505	1.525
11	1.450	1.460	1.470	1.490	1.510	1.530
12	1.455	1.465	1.475	1.495	1.515	1.535
13	1.460	1.470	1.480	1.500	1.520	1.540
14	1.465	1.475	1.485	1.505	1.525	1.545
15	1.470	1.480	1.490	1.510	1.530	1.550
16	1.475	1.485	1.495	1.515	1.535	1.555
17	1.480	1.490	1.500	1.520	1.540	1.560

Table SI1: *Wigner-Seitz radii indices* for Table SI2. For each index (I.), the Wigner-Seitz radius r_s is given for each temperature.

Table SI2: *Hellinger distances* for all MD-derived properties and benchmarked MLPs.

(a) *Yukawa potential*. Shown are HDs of pressures, stable molecular fractions, diffusion coefficients, and radial distribution functions (top to bottom) as functions of Wigner-Seitz radius (see Table SI1).

Pressures:

T/K	Index of Wigner-Seitz radius r_s																
	1	2	3	4	5	6	7	8	9	10	11	12	13	14	15	16	17
1000	1.00	1.00	1.00	1.00	1.00	1.00	1.00	1.00	1.00	1.00	1.00	1.00	1.00	1.00	1.00	1.00	1.00
1100	1.00	1.00	1.00	1.00	1.00	1.00	1.00	1.00	1.00	1.00	1.00	1.00	1.00	1.00	1.00	1.00	1.00
1200	1.00	1.00	1.00	1.00	1.00	1.00	1.00	1.00	1.00	1.00	1.00	1.00	1.00	1.00	1.00	1.00	1.00
1300	1.00	1.00	1.00	1.00	1.00	1.00	1.00	1.00	1.00	1.00	1.00	1.00	1.00	1.00	1.00	1.00	1.00
1400	1.00	1.00	1.00	1.00	1.00	1.00	1.00	1.00	1.00	1.00	1.00	1.00	1.00	1.00	1.00	1.00	1.00
1500	1.00	1.00	1.00	1.00	1.00	1.00	1.00	1.00	1.00	1.00	1.00	1.00	1.00	1.00	1.00	1.00	1.00

Stable molecular fractions:

T/K	Index of Wigner-Seitz radius r_s																
	1	2	3	4	5	6	7	8	9	10	11	12	13	14	15	16	17
1000	1.00	1.00	1.00	1.00	1.00	1.00	1.00	1.00	1.00	1.00	1.00	1.00	1.00	1.00	1.00	1.00	1.00
1100	1.00	1.00	1.00	1.00	1.00	1.00	1.00	1.00	1.00	1.00	1.00	1.00	1.00	1.00	1.00	1.00	1.00
1200	1.00	1.00	1.00	1.00	1.00	1.00	1.00	1.00	1.00	1.00	1.00	1.00	1.00	1.00	1.00	1.00	1.00
1300	1.00	1.00	1.00	1.00	1.00	1.00	1.00	1.00	1.00	1.00	1.00	1.00	1.00	1.00	1.00	1.00	1.00
1400	1.00	1.00	1.00	1.00	1.00	1.00	1.00	1.00	1.00	1.00	1.00	1.00	1.00	1.00	1.00	1.00	1.00
1500	1.00	1.00	1.00	1.00	1.00	1.00	1.00	1.00	1.00	1.00	1.00	1.00	1.00	1.00	1.00	1.00	1.00

Diffusion coefficients:

T/K	Index of Wigner-Seitz radius r_s																
	1	2	3	4	5	6	7	8	9	10	11	12	13	14	15	16	17
1000	0.91	0.97	0.98	0.91	1.00	1.00	1.00	1.00	1.00	1.00	1.00	1.00	1.00	1.00	1.00	1.00	1.00
1100	0.99	0.96	0.91	0.98	0.99	1.00	1.00	1.00	1.00	1.00	1.00	1.00	1.00	1.00	1.00	1.00	1.00
1200	0.95	0.78	1.00	0.96	0.97	1.00	1.00	1.00	1.00	1.00	1.00	1.00	1.00	1.00	1.00	1.00	1.00
1300	0.97	0.98	0.99	0.99	1.00	1.00	1.00	1.00	1.00	1.00	1.00	1.00	1.00	1.00	1.00	1.00	1.00
1400	0.94	1.00	0.99	1.00	0.98	0.99	1.00	0.99	1.00	1.00	1.00	1.00	1.00	1.00	1.00	1.00	1.00
1500	1.00	0.96	1.00	0.98	1.00	1.00	1.00	1.00	0.99	1.00	1.00	1.00	1.00	1.00	1.00	1.00	1.00

Radial distribution functions:

T/K	Index of Wigner-Seitz radius r_s																
	1	2	3	4	5	6	7	8	9	10	11	12	13	14	15	16	17
1000	0.78	0.79	0.79	0.79	0.77	0.78	0.76	0.78	0.78	0.79	0.79	0.79	0.81	0.80	0.79	0.79	0.79
1100	0.78	0.80	0.79	0.78	0.79	0.80	0.78	0.76	0.79	0.79	0.78	0.80	0.80	0.81	0.80	0.81	0.79
1200	0.78	0.79	0.79	0.78	0.79	0.79	0.81	0.77	0.80	0.79	0.80	0.79	0.80	0.80	0.82	0.81	0.79
1300	0.78	0.79	0.81	0.81	0.81	0.77	0.78	0.77	0.79	0.79	0.80	0.81	0.79	0.80	0.78	0.78	0.79
1400	0.80	0.80	0.80	0.82	0.77	0.79	0.79	0.78	0.79	0.80	0.81	0.80	0.81	0.79	0.80	0.81	0.80
1500	0.79	0.79	0.78	0.80	0.79	0.82	0.80	0.81	0.80	0.81	0.81	0.81	0.82	0.80	0.80	0.81	0.82

Table SI2: *Hellinger distances* (continued) for all MD-derived properties and benchmarked MLPs.

(b) *Tersoff potential*. Shown are HDs of pressures, stable molecular fractions, diffusion coefficients, and radial distribution functions (top to bottom) as functions of Wigner-Seitz radius (see Table SI1).

Pressures:

T/K	Index of Wigner-Seitz radius rs																
	1	2	3	4	5	6	7	8	9	10	11	12	13	14	15	16	17
1000	1.00	1.00	1.00	1.00	1.00	1.00	1.00	1.00	1.00	1.00	1.00	1.00	1.00	1.00	1.00	1.00	1.00
1100	1.00	1.00	1.00	1.00	1.00	1.00	1.00	1.00	1.00	1.00	1.00	1.00	1.00	1.00	1.00	1.00	1.00
1200	1.00	1.00	1.00	1.00	1.00	1.00	1.00	1.00	1.00	1.00	1.00	1.00	1.00	1.00	1.00	1.00	1.00
1300	1.00	1.00	1.00	1.00	1.00	1.00	1.00	1.00	1.00	1.00	1.00	1.00	1.00	1.00	1.00	1.00	1.00
1400	1.00	1.00	1.00	1.00	1.00	1.00	1.00	1.00	1.00	1.00	1.00	1.00	1.00	1.00	1.00	1.00	1.00
1500	1.00	1.00	1.00	1.00	1.00	1.00	1.00	1.00	1.00	1.00	1.00	1.00	1.00	1.00	1.00	1.00	1.00

Stable molecular fractions:

T/K	Index of Wigner-Seitz radius rs																
	1	2	3	4	5	6	7	8	9	10	11	12	13	14	15	16	17
1000	0.20	0.52	0.90	0.88	0.88	0.97	0.90	1.00	0.99	1.00	1.00	1.00	1.00	1.00	1.00	1.00	1.00
1100	0.30	0.92	0.76	0.98	0.94	0.99	0.96	0.93	0.99	1.00	1.00	1.00	1.00	1.00	1.00	1.00	1.00
1200	0.74	0.54	0.73	0.91	0.91	0.93	1.00	0.95	0.97	1.00	1.00	1.00	1.00	1.00	1.00	1.00	1.00
1300	0.95	0.99	1.00	0.83	0.99	0.99	0.98	0.98	0.99	0.99	1.00	1.00	1.00	1.00	1.00	1.00	1.00
1400	0.90	0.93	1.00	0.99	0.99	1.00	1.00	0.99	1.00	1.00	1.00	1.00	1.00	1.00	1.00	1.00	1.00
1500	0.96	1.00	1.00	1.00	1.00	1.00	1.00	1.00	1.00	1.00	1.00	1.00	1.00	1.00	1.00	1.00	1.00

Diffusion coefficients:

T/K	Index of Wigner-Seitz radius rs																
	1	2	3	4	5	6	7	8	9	10	11	12	13	14	15	16	17
1000	0.99	0.97	1.00	0.98	1.00	1.00	1.00	1.00	1.00	1.00	1.00	1.00	1.00	1.00	1.00	1.00	1.00
1100	0.99	0.96	0.99	0.98	0.99	1.00	1.00	1.00	1.00	1.00	1.00	1.00	1.00	1.00	1.00	1.00	1.00
1200	0.97	0.95	0.94	1.00	1.00	0.98	1.00	1.00	1.00	1.00	1.00	1.00	1.00	1.00	1.00	1.00	1.00
1300	0.99	1.00	0.99	1.00	0.98	1.00	0.92	1.00	1.00	1.00	1.00	1.00	1.00	1.00	1.00	1.00	1.00
1400	1.00	0.99	1.00	1.00	1.00	0.99	1.00	1.00	1.00	1.00	1.00	1.00	1.00	1.00	1.00	1.00	1.00
1500	0.99	0.97	1.00	0.98	1.00	1.00	1.00	0.99	1.00	1.00	1.00	1.00	1.00	1.00	1.00	1.00	1.00

Radial distribution functions:

T/K	Index of Wigner-Seitz radius rs																
	1	2	3	4	5	6	7	8	9	10	11	12	13	14	15	16	17
1000	0.86	0.87	0.87	0.85	0.84	0.90	0.85	0.89	0.87	0.88	0.89	0.91	0.92	0.91	0.91	0.92	0.94
1100	0.87	0.88	0.87	0.87	0.87	0.90	0.89	0.88	0.91	0.90	0.92	0.91	0.93	0.92	0.93	0.91	0.93
1200	0.88	0.89	0.87	0.87	0.90	0.90	0.92	0.89	0.90	0.92	0.91	0.91	0.94	0.94	0.93	0.94	0.94
1300	0.88	0.89	0.91	0.91	0.90	0.89	0.92	0.93	0.92	0.91	0.92	0.93	0.93	0.93	0.95	0.94	0.94
1400	0.90	0.90	0.90	0.92	0.90	0.92	0.90	0.90	0.92	0.93	0.94	0.93	0.93	0.94	0.94	0.95	0.96
1500	0.91	0.91	0.92	0.92	0.91	0.93	0.94	0.93	0.93	0.92	0.93	0.95	0.94	0.95	0.95	0.96	0.96

Table SI2: *Hellinger distances* (continued) for all MD-derived properties and benchmarked MLPs.

(c) *UFP2 potential*. Shown are HDs of pressures, stable molecular fractions, diffusion coefficients, and radial distribution functions (top to bottom) as functions of Wigner-Seitz radius (see Table SI1).

Pressures:

T/K	Index of Wigner-Seitz radius r_s																
	1	2	3	4	5	6	7	8	9	10	11	12	13	14	15	16	17
1000	1.00	1.00	1.00	1.00	1.00	1.00	1.00	1.00	1.00	1.00	1.00	1.00	1.00	1.00	1.00	1.00	1.00
1100	1.00	1.00	1.00	1.00	1.00	1.00	1.00	1.00	1.00	1.00	1.00	1.00	1.00	1.00	1.00	1.00	1.00
1200	1.00	1.00	1.00	1.00	1.00	1.00	1.00	1.00	1.00	1.00	1.00	1.00	1.00	1.00	1.00	1.00	1.00
1300	1.00	1.00	1.00	1.00	1.00	1.00	1.00	1.00	1.00	1.00	1.00	1.00	1.00	1.00	1.00	1.00	1.00
1400	1.00	1.00	1.00	1.00	1.00	1.00	1.00	1.00	1.00	1.00	1.00	1.00	1.00	1.00	1.00	1.00	1.00
1500	1.00	1.00	1.00	1.00	1.00	1.00	1.00	1.00	1.00	1.00	1.00	1.00	1.00	1.00	1.00	1.00	1.00

Stable molecular fractions:

T/K	Index of Wigner-Seitz radius r_s																
	1	2	3	4	5	6	7	8	9	10	11	12	13	14	15	16	17
1000	0.86	0.66	0.15	0.25	0.42	0.88	0.80	1.00	0.98	1.00	1.00	1.00	1.00	1.00	1.00	1.00	1.00
1100	0.88	0.37	0.13	0.04	0.58	0.87	0.87	0.82	0.97	0.99	1.00	1.00	1.00	1.00	1.00	1.00	1.00
1200	0.56	0.45	0.08	0.39	0.63	0.72	0.97	0.88	0.90	0.98	1.00	1.00	1.00	1.00	1.00	1.00	1.00
1300	0.10	0.77	0.92	0.65	0.96	0.95	0.91	0.94	0.97	0.98	0.99	1.00	1.00	1.00	1.00	1.00	1.00
1400	0.69	0.66	0.88	0.97	0.97	1.00	0.96	0.95	0.97	0.99	1.00	1.00	1.00	1.00	1.00	1.00	1.00
1500	0.81	0.99	0.92	0.90	0.94	1.00	1.00	0.99	1.00	1.00	1.00	1.00	1.00	1.00	1.00	1.00	1.00

Diffusion coefficients:

T/K	Index of Wigner-Seitz radius r_s																
	1	2	3	4	5	6	7	8	9	10	11	12	13	14	15	16	17
1000	0.10	0.35	0.45	0.37	0.70	0.88	0.76	1.00	1.00	1.00	1.00	1.00	1.00	1.00	1.00	1.00	1.00
1100	0.04	0.34	0.40	0.66	0.69	0.77	0.70	0.93	0.98	1.00	1.00	1.00	1.00	1.00	1.00	1.00	1.00
1200	0.22	0.28	0.32	0.55	0.63	0.46	0.74	0.94	0.79	1.00	1.00	1.00	1.00	0.99	1.00	1.00	1.00
1300	0.46	0.47	0.69	0.55	0.74	0.75	0.93	0.97	0.97	0.99	1.00	1.00	1.00	1.00	1.00	1.00	1.00
1400	0.46	0.79	0.81	0.97	0.78	0.92	0.99	0.93	1.00	1.00	1.00	1.00	1.00	1.00	1.00	1.00	1.00
1500	0.85	0.75	0.91	0.74	0.99	1.00	1.00	1.00	0.99	1.00	1.00	1.00	1.00	1.00	1.00	1.00	1.00

Radial distribution functions:

T/K	Index of Wigner-Seitz radius r_s																
	1	2	3	4	5	6	7	8	9	10	11	12	13	14	15	16	17
1000	0.65	0.62	0.61	0.60	0.58	0.52	0.45	0.57	0.56	0.63	0.69	0.68	0.68	0.65	0.69	0.71	0.69
1100	0.60	0.59	0.59	0.61	0.55	0.50	0.45	0.44	0.58	0.60	0.66	0.67	0.70	0.68	0.71	0.71	0.71
1200	0.58	0.54	0.54	0.50	0.48	0.47	0.47	0.50	0.57	0.59	0.65	0.67	0.70	0.70	0.71	0.73	0.74
1300	0.49	0.52	0.55	0.58	0.54	0.63	0.65	0.65	0.66	0.68	0.70	0.71	0.75	0.77	0.78	0.78	0.78
1400	0.64	0.65	0.66	0.69	0.71	0.70	0.69	0.68	0.72	0.73	0.74	0.76	0.77	0.78	0.78	0.80	0.80
1500	0.69	0.71	0.73	0.73	0.72	0.76	0.76	0.73	0.77	0.77	0.78	0.79	0.80	0.79	0.81	0.82	0.80

Table SI2: *Hellinger distances* (continued) for all MD-derived properties and benchmarked MLPs.

(d) *UFP3 potential*. Shown are HDs of pressures, stable molecular fractions, diffusion coefficients, and radial distribution functions (top to bottom) as functions of Wigner-Seitz radius (see Table SI1).

Pressures:

T/K	Index of Wigner-Seitz radius rs																
	1	2	3	4	5	6	7	8	9	10	11	12	13	14	15	16	17
1000	0.88	1.00	1.00	1.00	1.00	1.00	0.90	0.95	0.57	0.89	0.99	1.00	1.00	1.00	1.00	1.00	1.00
1100	1.00	1.00	1.00	1.00	1.00	1.00	1.00	1.00	0.99	0.93	0.91	1.00	1.00	1.00	1.00	1.00	1.00
1200	1.00	1.00	1.00	1.00	1.00	1.00	1.00	1.00	1.00	1.00	0.94	0.98	1.00	1.00	1.00	1.00	1.00
1300	1.00	1.00	1.00	1.00	1.00	1.00	1.00	1.00	1.00	1.00	0.98	0.98	1.00	1.00	1.00	1.00	1.00
1400	1.00	1.00	1.00	1.00	1.00	1.00	1.00	0.99	0.98	1.00	1.00	1.00	1.00	1.00	1.00	1.00	1.00
1500	1.00	1.00	1.00	1.00	1.00	1.00	1.00	1.00	1.00	1.00	1.00	1.00	1.00	1.00	1.00	1.00	1.00

Stable molecular fractions:

T/K	Index of Wigner-Seitz radius rs																
	1	2	3	4	5	6	7	8	9	10	11	12	13	14	15	16	17
1000	1.00	1.00	1.00	0.97	0.94	0.50	0.44	0.83	0.71	1.00	1.00	1.00	1.00	1.00	1.00	1.00	1.00
1100	1.00	1.00	1.00	1.00	0.98	0.99	0.54	0.43	0.52	0.81	0.94	1.00	1.00	1.00	1.00	1.00	1.00
1200	0.99	1.00	1.00	1.00	0.99	1.00	1.00	0.46	0.46	0.54	0.87	0.99	1.00	1.00	1.00	1.00	1.00
1300	1.00	0.97	1.00	1.00	0.99	0.93	0.48	0.33	0.59	0.64	0.84	0.94	1.00	1.00	1.00	1.00	1.00
1400	1.00	1.00	0.99	0.98	0.96	0.82	0.29	0.57	0.71	0.87	0.97	1.00	1.00	1.00	1.00	1.00	1.00
1500	0.99	0.86	0.83	0.54	0.17	0.24	0.92	0.83	0.92	1.00	1.00	1.00	1.00	1.00	1.00	1.00	1.00

Diffusion coefficients:

T/K	Index of Wigner-Seitz radius rs																
	1	2	3	4	5	6	7	8	9	10	11	12	13	14	15	16	17
1000	0.56	0.66	0.95	0.38	0.54	0.20	0.27	0.80	0.71	0.95	0.92	0.99	0.95	1.00	0.65	0.99	0.63
1100	0.80	0.55	0.67	0.79	0.47	0.40	0.08	0.02	0.35	0.38	0.78	0.98	1.00	1.00	0.94	0.88	0.93
1200	0.60	0.64	0.53	0.61	0.54	0.41	0.26	0.01	0.01	0.34	0.84	0.97	0.99	1.00	1.00	0.94	0.91
1300	0.70	0.04	0.41	0.99	0.40	0.39	0.13	0.22	0.54	0.44	0.62	0.93	0.95	1.00	1.00	1.00	0.99
1400	0.47	0.58	0.51	0.28	0.16	0.13	0.11	0.29	0.28	0.52	0.84	1.00	0.99	0.99	1.00	1.00	1.00
1500	0.26	0.13	0.32	0.04	0.05	0.32	0.86	0.80	0.83	0.97	1.00	1.00	1.00	1.00	1.00	0.98	1.00

Radial distribution functions:

T/K	Index of Wigner-Seitz radius rs																
	1	2	3	4	5	6	7	8	9	10	11	12	13	14	15	16	17
1000	0.60	0.57	0.59	0.59	0.58	0.55	0.36	0.30	0.26	0.38	0.36	0.35	0.47	0.46	0.52	0.50	0.42
1100	0.60	0.61	0.65	0.62	0.61	0.63	0.57	0.55	0.36	0.32	0.37	0.38	0.49	0.50	0.50	0.55	0.54
1200	0.67	0.64	0.66	0.66	0.67	0.66	0.68	0.60	0.52	0.49	0.44	0.48	0.52	0.54	0.52	0.56	0.58
1300	0.66	0.65	0.67	0.71	0.67	0.66	0.66	0.59	0.55	0.51	0.53	0.55	0.60	0.60	0.66	0.65	0.68
1400	0.69	0.69	0.72	0.71	0.69	0.73	0.59	0.58	0.52	0.57	0.59	0.63	0.64	0.70	0.69	0.74	0.74
1500	0.71	0.70	0.71	0.69	0.66	0.67	0.61	0.59	0.63	0.71	0.70	0.73	0.74	0.76	0.78	0.77	0.77

Table SI2: *Hellinger distances* (continued) for all MD-derived properties and benchmarked MLPs.

(e) *PACE potential*. Shown are HDs of pressures, stable molecular fractions, diffusion coefficients, and radial distribution functions (top to bottom) as functions of Wigner-Seitz radius (see Table SI1).

Pressures:

T/K	Index of Wigner-Seitz radius r_s																
	1	2	3	4	5	6	7	8	9	10	11	12	13	14	15	16	17
1000	0.90	0.97	0.93	0.69	0.92	0.34	0.47	0.88	0.68	1.00	1.00	1.00	0.98	0.96	0.64	0.62	0.22
1100	1.00	0.99	1.00	0.99	1.00	0.97	0.43	0.49	0.36	0.71	0.75	1.00	1.00	1.00	0.99	0.90	0.67
1200	1.00	1.00	1.00	1.00	0.93	0.98	1.00	0.77	0.57	0.16	0.54	0.80	0.92	1.00	0.99	0.99	0.96
1300	1.00	1.00	1.00	1.00	1.00	0.94	1.00	0.61	0.37	0.23	0.46	0.70	1.00	0.93	1.00	1.00	1.00
1400	1.00	1.00	1.00	1.00	1.00	1.00	0.55	0.59	0.45	0.40	0.78	0.96	1.00	1.00	1.00	1.00	1.00
1500	1.00	1.00	1.00	1.00	0.78	1.00	0.12	0.40	0.81	0.99	1.00	1.00	1.00	1.00	1.00	1.00	1.00

Stable molecular fractions:

T/K	Index of Wigner-Seitz radius r_s																
	1	2	3	4	5	6	7	8	9	10	11	12	13	14	15	16	17
1000	0.25	0.21	0.47	0.33	0.49	0.81	0.73	0.99	0.93	1.00	1.00	1.00	1.00	1.00	1.00	1.00	1.00
1100	0.03	0.18	0.04	0.04	0.21	0.35	0.57	0.66	0.89	0.94	0.98	1.00	1.00	1.00	1.00	1.00	1.00
1200	0.12	0.28	0.03	0.06	0.02	0.18	0.10	0.33	0.50	0.78	0.94	1.00	1.00	1.00	1.00	1.00	1.00
1300	0.14	0.29	0.37	0.27	0.66	0.04	0.15	0.61	0.79	0.75	0.83	0.92	1.00	1.00	1.00	1.00	1.00
1400	0.42	0.84	0.71	0.45	0.26	0.09	0.40	0.62	0.68	0.76	0.92	0.99	1.00	1.00	0.99	1.00	1.00
1500	0.59	0.21	0.54	0.42	0.15	0.03	0.73	0.71	0.80	0.98	1.00	1.00	1.00	1.00	1.00	1.00	1.00

Diffusion coefficients:

T/K	Index of Wigner-Seitz radius r_s																
	1	2	3	4	5	6	7	8	9	10	11	12	13	14	15	16	17
1000	0.19	0.48	0.40	0.51	0.53	0.64	0.41	0.97	0.98	1.00	1.00	1.00	1.00	1.00	0.92	0.99	0.85
1100	0.27	0.23	0.19	0.22	0.45	0.38	0.40	0.31	0.72	0.80	0.96	1.00	1.00	1.00	0.98	0.97	0.90
1200	0.04	0.01	0.04	0.20	0.08	0.06	0.18	0.42	0.39	0.67	1.00	1.00	0.86	0.98	0.99	0.93	0.79
1300	0.31	0.18	0.30	0.16	0.01	0.15	0.06	0.67	0.76	0.58	0.83	0.81	0.99	0.98	0.98	0.99	0.95
1400	0.04	0.13	0.10	0.20	0.10	0.09	0.29	0.39	0.46	0.66	0.77	0.95	0.95	0.95	0.96	0.97	0.96
1500	0.20	0.23	0.19	0.01	0.06	0.24	0.70	0.94	0.59	1.00	0.96	0.85	0.95	0.88	0.85	0.75	0.98

Radial distribution functions:

T/K	Index of Wigner-Seitz radius r_s																
	1	2	3	4	5	6	7	8	9	10	11	12	13	14	15	16	17
1000	0.10	0.19	0.10	0.13	0.12	0.27	0.27	0.54	0.51	0.58	0.63	0.60	0.59	0.51	0.44	0.59	0.44
1100	0.10	0.06	0.07	0.08	0.07	0.12	0.14	0.12	0.39	0.45	0.55	0.61	0.56	0.51	0.53	0.46	0.43
1200	0.17	0.12	0.16	0.12	0.13	0.12	0.14	0.08	0.14	0.23	0.41	0.49	0.49	0.54	0.48	0.47	0.45
1300	0.21	0.20	0.19	0.27	0.25	0.15	0.12	0.12	0.20	0.23	0.31	0.41	0.49	0.41	0.50	0.38	0.33
1400	0.27	0.32	0.29	0.26	0.23	0.17	0.11	0.14	0.19	0.19	0.29	0.38	0.39	0.37	0.38	0.39	0.31
1500	0.25	0.23	0.33	0.29	0.18	0.18	0.12	0.21	0.29	0.43	0.41	0.45	0.39	0.39	0.42	0.40	0.35

Table SI2: *Hellinger distances* (continued) for all MD-derived properties and benchmarked MLPs.

(f) *MACE potential*. Shown are HDs of pressures, stable molecular fractions, diffusion coefficients, and radial distribution functions (top to bottom) as functions of Wigner-Seitz radius (see Table SI1).

Pressures:

T/K	Index of Wigner-Seitz radius rs																
	1	2	3	4	5	6	7	8	9	10	11	12	13	14	15	16	17
1000	0.41	0.49	0.15	0.05	0.06	0.02	0.14	0.17	0.17	0.32	0.16	0.40	0.39	0.37	0.41	0.01	0.02
1100	0.03	0.11	0.13	0.01	0.02	0.01	0.00	0.12	0.23	0.08	0.09	0.30	0.22	0.31	0.33	0.17	0.06
1200	0.18	0.16	0.13	0.06	0.19	0.28	0.00	0.17	0.06	0.13	0.61	0.35	0.25	0.63	0.27	0.30	0.38
1300	0.36	0.10	0.10	0.18	0.21	0.00	0.03	0.09	0.17	0.12	0.05	0.17	0.78	0.22	0.44	0.38	0.49
1400	0.52	0.59	0.25	0.28	0.24	0.17	0.13	0.13	0.19	0.12	0.34	0.21	0.40	0.44	0.27	0.61	0.50
1500	0.11	0.14	0.41	0.07	0.04	0.23	0.41	0.17	0.34	0.73	0.74	0.77	0.80	0.85	0.80	0.88	0.95

Stable molecular fractions:

T/K	Index of Wigner-Seitz radius rs																
	1	2	3	4	5	6	7	8	9	10	11	12	13	14	15	16	17
1000	0.21	0.11	0.16	0.17	0.00	0.05	0.26	0.18	0.26	0.34	0.34	0.35	0.16	0.26	0.37	0.00	0.00
1100	0.03	0.23	0.03	0.19	0.19	0.03	0.03	0.22	0.39	0.07	0.11	0.29	0.24	0.24	0.12	0.12	0.01
1200	0.16	0.12	0.06	0.13	0.26	0.11	0.11	0.34	0.22	0.22	0.67	0.41	0.32	0.64	0.23	0.20	0.33
1300	0.06	0.26	0.09	0.21	0.02	0.16	0.20	0.33	0.21	0.27	0.07	0.17	0.66	0.23	0.46	0.13	0.27
1400	0.09	0.23	0.04	0.02	0.00	0.17	0.32	0.30	0.27	0.18	0.28	0.20	0.30	0.28	0.07	0.24	0.50
1500	0.01	0.16	0.01	0.03	0.01	0.07	0.41	0.17	0.31	0.63	0.62	0.49	0.39	0.27	0.30	0.42	0.42

Diffusion coefficients:

T/K	Index of Wigner-Seitz radius rs																
	1	2	3	4	5	6	7	8	9	10	11	12	13	14	15	16	17
1000	0.20	0.21	0.33	0.07	0.13	0.10	0.05	0.25	0.24	0.38	0.04	0.24	0.16	0.20	0.13	0.03	0.10
1100	0.09	0.13	0.24	0.13	0.26	0.22	0.03	0.14	0.16	0.01	0.05	0.40	0.36	0.13	0.17	0.13	0.03
1200	0.09	0.01	0.01	0.16	0.07	0.01	0.26	0.11	0.10	0.42	0.62	0.32	0.22	0.17	0.19	0.04	0.18
1300	0.38	0.22	0.16	0.28	0.05	0.23	0.14	0.57	0.47	0.20	0.02	0.15	0.25	0.32	0.11	0.38	0.09
1400	0.03	0.25	0.06	0.11	0.10	0.00	0.02	0.11	0.07	0.11	0.06	0.41	0.20	0.11	0.15	0.23	0.27
1500	0.15	0.28	0.14	0.06	0.07	0.24	0.69	0.17	0.12	0.72	0.59	0.33	0.30	0.11	0.11	0.07	0.31

Radial distribution functions:

T/K	Index of Wigner-Seitz radius rs																
	1	2	3	4	5	6	7	8	9	10	11	12	13	14	15	16	17
1000	0.08	0.08	0.07	0.07	0.06	0.05	0.08	0.11	0.15	0.19	0.09	0.15	0.22	0.20	0.19	0.08	0.07
1100	0.09	0.06	0.07	0.08	0.05	0.07	0.05	0.07	0.15	0.05	0.09	0.18	0.15	0.15	0.11	0.16	0.04
1200	0.06	0.06	0.06	0.05	0.07	0.07	0.10	0.06	0.11	0.16	0.31	0.17	0.13	0.17	0.11	0.08	0.11
1300	0.05	0.06	0.07	0.06	0.06	0.10	0.09	0.11	0.14	0.12	0.07	0.12	0.22	0.11	0.10	0.10	0.09
1400	0.05	0.08	0.05	0.05	0.04	0.07	0.07	0.09	0.11	0.08	0.11	0.10	0.10	0.09	0.06	0.11	0.09
1500	0.07	0.12	0.07	0.05	0.07	0.09	0.12	0.11	0.13	0.27	0.16	0.18	0.16	0.09	0.12	0.14	0.13

References

1. Paolo Giannozzi, Stefano Baroni, Nicola Bonini, Matteo Calandra, Roberto Car, Carlo Cavazzoni, Davide Ceresoli, Guido L. Chiarotti, Matteo Cococcioni, Ismaila Dabo, et al.: *QUANTUM ESPRESSO: a modular and open-source software project for quantum simulations of materials*. Journal of Physics: Condensed Matter 21(39): 395502, 2009.
2. John P. Perdew, Kieron Burke, Matthias Ernzerhof: *Generalized gradient approximation made simple*. Physical Review Letters 77(18): 3865, 1996.
3. Andrea Dal Corso: *Pseudopotentials periodic table: From H to Pu*. Computational Materials Science 95: 337, 2014.
4. Walter Kohn, Lu J. Sham: *Self-consistent equations including exchange and correlation effects*. Physical Review 140(4A): A1133, 1965.
5. Hua Y. Geng, Q. Wu, Miriam Marqués, Graeme J. Ackland: *Thermodynamic anomalies and three distinct liquid-liquid transitions in warm dense liquid hydrogen*. Physical Review B 100(13): 134109, 2019.
6. Bingqing Cheng, Guglielmo Mazzola, Chris J. Pickard, Michele Ceriotti: *Evidence for supercritical behaviour of high-pressure liquid hydrogen*. Nature 585(7824): 217, 2020.
7. Andrea Tirelli, Giacomo Tenti, Kousuke Nakano, Sandro Sorella: *High-pressure hydrogen by machine learning and quantum Monte Carlo*. Physical Review B 106(4): L041105, 2022.
8. Hongwei Niu, Yubo Yang, Scott Jensen, Markus Holzmann, Carlo Pierleoni, David M. Ceperley: *Stable solid molecular hydrogen above 900 K from a machine-learned potential trained with diffusion quantum Monte Carlo*. Physical Review Letters 130(7): 076102, 2023.
9. Valentin V. Karasiev, Joshua Hinz, Suxing Hu, Samuel B. Trickey: *On the liquid-liquid phase transition of dense hydrogen*. Nature 600(7889): E12, 2021.
10. Aidan P. Thompson, H. Metin Aktulga, Richard Berger, Dan S. Bolintineanu, Miachel W. Brown, Paul S. Crozier, Pieter J. in't Veld, Axel Kohlmeyer, Stan G. Moore, Trung Dac Nguyen, et al.: *LAMMPS—a flexible simulation tool for particle-based materials modeling at the atomic, meso, and continuum scales*. Computer Physics Communications 271: 108171, 2022.
11. Giovanni Bussi, Davide Donadio, Michele Parrinello: *Canonical sampling through velocity rescaling*. The Journal of Chemical Physics 126(1): 014101, 2007.
12. Winfried Lorenzen, Bastian Holst, Ronald Redmer: *First-order liquid-liquid phase transition in dense hydrogen*. Physical Review B 82(19): 195107, 2010.
13. Miguel A. Morales, Carlo Pierleoni, Eric Schwegler, David M. Ceperley: *Evidence for a first-order liquid-liquid transition in high-pressure hydrogen from ab initio simulations*. Proceedings of the National Academy of Sciences of the United States of America 107(29): 12799, 2010.
14. Guglielmo Mazzola, Ravit Helled, Sandro Sorella: *Phase diagram of hydrogen and a hydrogen-helium mixture at planetary conditions by quantum Monte Carlo simulations*. Physical Review Letters 120(2): 025701, 2018.
15. Joshua Hinz, Valentin V. Karasiev, Su Xing Hu, Mohamed Zaghoo, Daniel Mejía-Rodríguez, Samuel B. Trickey, Lucas Calderín: *Fully consistent density functional theory determination of the insulator-metal transition boundary in warm dense hydrogen*. Physical Review Research 2(3): 032065(R), 2020.
16. Jianwei Sun, Adrienn Ruzsinszky, John P. Perdew: *Strongly constrained and appropriately normed semilocal density functional*. Physical Review Letters 115(3): 036402, 2015.
17. John A. Nelder, Roger Mead: *A simplex method for function minimization*. The Computer Journal 7(4): 308, 1965.
18. Pauli Virtanen, Ralf Gommers, Travis E. Oliphant, Matt Haberland, Tyler Reddy, David Cournapeau, Evgeni Burovski, Pearu Peterson, Warren Weckesser, Jonathan Bright, et al.: *SciPy 1.0: fundamental algorithms for scientific computing in python*. Nature Methods 17(3): 261, 2020.

19. Yury Lysogorskiy, Cas van der Oord, Anton Bochkarev, Sarath Menon, Matteo Rinaldi, Thomas Hammerschmidt, Matous Mrovec, Aidan P. Thompson, Gábor Csányi, Christoph Ortner, et al.: *Performant implementation of the atomic cluster expansion (PACE) and application to copper and silicon*. npj Computational Materials 7: 97, 2021.
20. Anton Bochkarev, Yury Lysogorskiy, Sarath Menon, Minaam Qamar, Matous Mrovec, Ralf Drautz: *Efficient parametrization of the atomic cluster expansion*. Physical Review Materials 6(1): 013804, 2022.